Studying the Multi-frequency Angular Power Spectrum of the Cosmic Dawn 21-cm Signal

Abinash Kumar Shaw, Raghunath Ghara, Saleem Zaroubi, Rajesh Mondal, Garrelt Mellema, Florent Mertens, Léon V.E. Koopmans, Benoît Semelin

Monthly Notices of the ROYAL ASTRONOMICAL SOCIETY

MNRAS **522,** 2188–2206 (2023) https://doi.org/10.1093/mnras/stad1114
Advance Access publication 2023 April 14

Studying the multifrequency angular power spectrum of the cosmic dawn 21-cm signal

Abinash Kumar Shaw [1]★ Raghunath Ghara [1] Saleem Zaroubi [2,3] Rajesh Mondal [4,5] Garrelt Mellema [5] Florent Mertens [3,6] Léon V. E. Koopmans [3] and Benoît Semelin [6]

[1]*Astrophysics Research Center of the Open University (ARCO), The Open University of Israel, 1 University Road, Ra'anana 4353701, Israel*
[2]*Department of Natural Sciences, The Open University of Israel, 1 University Road, Ra'anana 4353701, Israel*
[3]*Kapteyn Astronomical Institute, University of Groningen, PO Box 800, NL-9700AV Groningen, the Netherlands*
[4]*Department of Astrophysics, School of Physics and Astronomy, Tel Aviv University, Tel Aviv 69978, Israel*
[5]*Department of Astronomy & Oskar Klein Centre, Stockholm University, AlbaNova, SE-10691 Stockholm, Sweden*
[6]*LERMA, Observatoire de Paris, PSL Research University, CNRS, Sorbonne Université, F-75014 Paris, France*

Accepted 2023 April 12. Received 2023 April 8; in original form 2023 February 2

ABSTRACT

The light-cone (LC) anisotropy arises due to cosmic evolution of the cosmic dawn (CD) 21-cm signal along the line-of-sight (LoS) axis of the observation volume. The LC effect makes the signal statistically non-ergodic along the LoS axis. The multifrequency angular power spectrum (MAPS) provides an unbiased alternative to the popular three-dimensional (3D) power spectrum as it does not assume statistical ergodicity along every direction in the signal volume. Unlike the 3D power spectrum which mixes the cosmic evolution of the 21-cm signal along the LoS k modes, MAPS keeps the evolution information disentangled. Here, we first study the impact of different underlying physical processes during CD on the behaviour of the 21-cm MAPS using simulations of various different scenarios and models. We also make error predictions in 21-cm MAPS measurements considering only the system noise and cosmic variance for mock observations of *Hydrogen Epoch of Reionization Array* (*HERA*), *NenuFAR*, and *SKA-Low*. We find that 100 h of *HERA* observations will be able to measure 21-cm MAPS at $\geq 3\sigma$ for $\ell \lesssim 1000$ with 0.1 MHz channel-width. The better sensitivity of *SKA-Low* allows reaching this sensitivity up to $\ell \lesssim 3000$. Note that due to the difference in the frequency coverage of the various experiments, the CD–epoch of reionization model considered for *NenuFAR* is different than those used for the *HERA* and *SKA-Low* predictions. Considering *NenuFAR* with the new model, measurements $\geq 2\sigma$ are possible only for $\ell \lesssim 600$ with 0.2 MHz channel-width and for a 10 times longer observation time of $t_{\rm obs} = 1000$ h. However, for the range $300 \lesssim \ell \lesssim 600$ and $t_{\rm obs} = 1000$ h more than 3σ measurements are still possible for *NenuFAR* when combining consecutive frequency channels within a 5 MHz band.

Key words: *(cosmology:)* dark ages, reionization, first stars – *(cosmology:)* diffuse radiation – *(cosmology:)* large-scale structure of Universe – cosmology: observations – cosmology: theory – methods: statistical.

1 INTRODUCTION

The study of cosmic dawn (CD) and epoch of reionization (EoR) is very crucial to understand the first luminous objects in our Universe and how they caused the last important phase change in the intergalactic medium (IGM) on cosmological scales. X-ray emission from these first objects (stars, quasars, etc.) are expected to heat up the cold neutral hydrogen atom (H I) during the CD which is then followed by ultraviolet (UV) photoionization of H I during the EoR (see e.g. Pritchard & Furlanetto 2007; Zaroubi 2013; Shaw et al. 2023, for reviews). Unfortunately, our current understanding of the IGM during the EoR is limited to only a few indirect observations such as the measurements of Thomson scattering optical depth of the cosmic microwave background (CMB) photons with the free electrons (e.g. Planck Collaboration VI 2020) and the presence of complete Gunn–Peterson troughs in high-redshift quasar spectra (e.g. Becker et al. 2001, 2015; Fan et al. 2006; Gallerani, Choudhury & Ferrara 2006). Furthermore, results from the observations of high-redshift Ly-α emitters (e.g. Hu et al. 2010; Ota et al. 2017; Ishigaki et al. 2018; Morales et al. 2021), the Ly-α damping wings in high-redshift quasar spectra (e.g. Bañados et al. 2018; Davies et al. 2018; Ďurovčíková et al. 2020; Reiman et al. 2020; Wang et al. 2020; Yang et al. 2020; Greig et al. 2022), Lyman break galaxies (Mason et al. 2018; Hoag et al. 2019; Naidu et al. 2020), the measurements of the effective optical depth of the Ly-α (and Ly-β) forests (e.g. McGreer, Mesinger & D'Odorico 2014; Kulkarni et al. 2019; Raste et al. 2021; Zhu et al. 2021, 2022), and the high-z Ly-α emitters clustering measurements (e.g. Faisst et al. 2014; Sobacchi & Mesinger 2015; Santos, Sobral & Matthee 2016; Wold et al. 2022) have put some lose bounds on the average H I fraction in the IGM. These indirect observations in combination suggest a bound on the timing of reionization to be between redshift (z) $\approx$5.5 and $\approx$12 (e.g. Robertson et al. 2015; Mitra, Choudhury & Ratra 2018; Dai et al.

★ E-mail: abinashkumarshaw@gmail.com

2019; Qin et al. 2021). Besides the ionization state, there have been attempts to constrain IGM temperature and photoionization rates using Ly-α forests observations (Gaikwad et al. 2020). However, these constraints are not very tight and a direct probe of the IGM is required to answer several fundamental questions regarding CD–EoR such as what is the exact duration of these epochs, how the heating and reionization have progressed, what were the sources involved and what were their properties.

The most promising direct probe to the CD–EoR is the redshifted 21-cm radiation which is emitted due to hyperfine transition of H I in the IGM (e.g. Wouthuysen 1952; Field 1958; Sunyaev & Zeldovich 1972; Hogan & Rees 1979; Scott & Rees 1990; Bharadwaj & Sethi 2001). Concerted efforts have been put into observing the brightness temperature fluctuations of the redshifted 21-cm signal using low frequency radio-interferometers. Several current telescopes, such as *LOFAR*[1] (van Haarlem et al. 2013), *PAPER*[2] (Parsons et al. 2010), *NenuFAR*[3] (Zarka et al. 2018), *uGMRT*[4] (Swarup et al. 1991; Gupta et al. 2017), *MWA*[5] (Tingay et al. 2013), and *Hydrogen Epoch of Reionization Array* (*HERA*, DeBoer et al. 2017)[6] are trying to measure the redshifted 21-cm signal statistically.

Despite these efforts, the 21-cm signal has not yet been measured due to several observational challenges. The cosmological 21-cm signal is 10^4–10^5 times weaker than the galactic and extra-galactic foregrounds (e.g. Ali, Bharadwaj & Chengalur 2008; Bernardi et al. 2009, 2010; Ghosh et al. 2012; Beardsley et al. 2016). In addition, the system noise, systematics and calibration errors, and the human-made radio-frequency interference pose a challenge to the direct detection of the CD–EoR 21-cm signal. However, recent improvements in the foreground mitigation methods (e.g. Datta, Bowman & Carilli 2010; Mertens, Ghosh & Koopmans 2018; Hothi et al. 2020) and calibration techniques (e.g. Kern et al. 2019; Mevius et al. 2021; Gan et al. 2023) have led us to useful upper limits on spherically averaged three-dimensional (3D) power spectrum [e.g. *LOFAR* (Patil et al. 2017; Gehlot et al. 2019; Mertens et al. 2020), *GMRT* (Paciga et al. 2011, 2013), *MWA* (Li et al. 2019; Trott et al. 2020), *PAPER* (Cheng et al. 2018; Kolopanis et al. 2019), *HERA* (Abdurashidova et al. 2022; The HERA Collaboration et al. 2022), and *OVRO-LWA* (Eastwood et al. 2019)]. Despite these challenges, the upper limits are constantly improving and a few recent upper limits have started ruling out extreme models of the high-z IGM [e.g. *LOFAR* (Ghara et al. 2020; Greig et al. 2020b; Mondal et al. 2020b), *MWA* (Greig et al. 2020a; Ghara et al. 2021), and *HERA* (Abdurashidova et al. 2022; The HERA Collaboration et al. 2022)]. The upcoming *SKA-Low*[7] is expected to measure the 21-cm 3D power spectrum from both CD and EoR within about a 100 h of observing time (e.g. Koopmans et al. 2014; Shaw, Bharadwaj & Mondal 2019). *SKA-Low* will also be able to produce images of 21-cm signals during CD (Ghara et al. 2016) and EoR (Mellema et al. 2013) within a 1000 h of observing time.

These radio-interferometric observations record the 3D distribution of the H I 21-cm signal, where the third direction in the data volume is constructed from several channels across the frequency bandwidth. The 21-cm signal measured at different frequencies corresponds to the signal originating at different redshifts and thereby at different cosmic times. Thus, the imprint of cosmic evolution in the data makes the observed 21-cm signal statistically non-ergodic along the frequency axis. This effect, also known as the 'light-cone (LC) effect' is inevitable in any line-intensity mapping observations. Barkana & Loeb (2006) were the first to analytically quantify the line-of-sight (LoS) anisotropy introduced in the EoR 21-cm signal due to the LC effect. The LC effect also biases the statistical estimators which assume statistical ergodicity and periodicity in the data in all directions such as 3D N-point correlation functions and their Fourier conjugates. Several studies have quantified the LC effect on the two-point correlations (Zawada et al. 2014) and the 3D power spectrum (e.g. Datta et al. 2012, 2014; Plante et al. 2014) using the numerically simulated EoR 21-cm signal. Datta et al. (2012) found that the effect is about 50 per cent on scales corresponding to $k = 0.08\,\mathrm{Mpc}^{-1}$ along the LoS. Datta et al. (2014) found that the LC effect shows dramatic changes in 3D power spectrum only during the initial ($\bar{x}_{\rm HI} \approx 0.2$) and final ($\bar{x}_{\rm HI} \approx 0.8$) stages of their fiducial reionization model. However, they also argue that impact would be more important for shorter reionization histories. Ghara, Datta & Choudhury (2015b) are the first to study the effect of LC anisotropy on CD 21-cm 3D power spectra. They concluded that the LC effects are important for the CD 21-cm signal which is mostly governed by the spin temperature fluctuations that in turn are controlled by inhomogeneous X-ray heating and the Ly-α coupling of the IGM. They reported suppression(enhancement) in the peaks(dips) by factors $\geq$0.6(2.0) for their fiducial model at large scales ($k \approx 0.05\,\mathrm{Mpc}^{-1}$) using simulated LC boxes having volume $V = [200\ h^{-1}\,\mathrm{Mpc}]^3$. Unlike during the EoR, the LC bias becomes dramatically important during CD, even at small scales ($k \sim 1\,\mathrm{Mpc}^{-1}$).

Recently, Mondal, Bharadwaj & Datta (2018) have proposed the use of multifrequency angular power spectrum (MAPS) to evade the issue of the LC effect in the EoR 21-cm signal while quantifying its two-point statistics. Unlike the 3D power spectrum, MAPS is a non-stationary estimator along the LoS axis that captures the two-point statistics without any bias originating due to LC anisotropy in the observed signal. MAPS also has potential to recover the evolution of EoR (Mondal et al. 2019). Later, Mondal et al. (2020a) have quantified the EoR 21-cm MAPS and predicted its detectability in context of future *SKA-Low* observations. Recently, Trott et al. (2022) have produced first upper limits on the EoR 21-cm MAPS within $z = 6.2$–7.5 using the *MWA* data. MAPS statistics is expected to contain more unbiased information of the 21-cm signal than 3D power spectrum. This extra information can be exploited to put more stringent constraints over the models of CD–EoR (Mondal et al. 2022). Along a similar line, this work focuses on estimating the CD 21-cm MAPS using a suite of CD–EoR 21-cm simulations. We aim to predict the detectability of CD 21-cm MAPS using several current (*HERA* and *NenuFAR*) and upcoming (*SKA-Low*) telescopes. Unlike recent works which were limited to estimating the EoR 21-cm MAPS within a small frequency bandwidth (LoS depth $\lesssim$ 1 Gpc), here we have computed 21-cm MAPS over a large frequency bandwidth (LoS depth $\approx$ 2.1 Gpc; redshift range $z \approx$ 6–19) that comprises both the CD and EoR.

The organization of this paper is as follows. Section 2 briefly describes the simulation methodology, the impact of LC effect on CD–EoR 21-cm 3D power spectrum and the formulation and implementation of the MAPS statistics. We then discuss the theoretical implications of different physical processes and source models on 21-cm MAPS in Section 3. In Section 4, we discuss the detectability of the CD–EoR 21-cm MAPS considering *HERA*, *NenuFAR*, and *SKA-Low* telescopes. Finally, we summarize our work and conclude

[1] https://www.astron.nl/telescopes/lofar
[2] http://eor.berkeley.edu
[3] https://nenufar.obs-nancay.fr/en/homepage-en
[4] http://www.gmrt.ncra.tifr.res.in
[5] https://www.mwatelescope.org
[6] https://reionization.org
[7] https://www.skao.int

in Section 5. This work uses the cosmological parameter values $\Omega_m = 0.27$, $\Omega_\Lambda = 0.73$, $\Omega_B = 0.044$, and $h = 0.7$ taken from Hinshaw et al. (2013). These parameters have been used in the *N*-body simulation for this work.

2 METHODOLOGY

We first briefly describe our LC simulations in this section. Next, we study the impact of the LC effect on the 3D power spectrum estimator using our LC simulation. Finally, we describe the machinery of MAPS after motivating it as an alternative to the 3D power spectrum.

2.1 Simulating the 21-cm signal LC

We use the GRIZZLY code (Ghara, Choudhury & Datta 2015a; Ghara et al. 2018) to simulate 21-cm signal coeval cubes at different redshifts during the CD and EoR. This code is based on a 1D radiative transfer method which takes the cosmological density and velocity fields and the halo catalogues as input to simulate the differential brightness temperature (δT_b) coeval cubes of the 21-cm signal for a source model. Later, we use these coeval δT_b cubes to generate a δT_b LC that spans the CD and EoR. Here, we briefly describe the steps employed to generate the 21-cm signal LCs which we will use in this study.

The cosmological density and velocity fields and the halo catalogues, used in this study, are taken from results of the PRACE[8] project PRACE4LOFAR. These inputs are from a dark matter only *N*-body simulation that was run using the code CUBEP^{3}M[9] (Harnois-Déraps et al. 2013). Here, we use gridded density and velocity fields in 3D comoving cubes with length 500 h^{-1} comoving megaparsec (Mpc) (see e.g. Dixon et al. 2015; Giri et al. 2019). The volume is gridded into 300^3 cubical voxels. We use 59 snapshots in the redshift range $20 \gtrsim z \gtrsim 6.5$ in equal time-steps of 11.4 Myr. The dark matter haloes were identified using a spherical overdensity halo finder (Watson et al. 2013). The minimum mass of the dark matter haloes is $\sim 10^9$ $M_\odot$, having at least ≈25 dark matter particles.

The source model used in this study assumes that each dark matter halo with mass larger than 10^9 $M_\odot$ hosts sources which emit UV as well as X-rays. In particular, we consider a combination of galaxy and mini-quasar type sources. We assume that the stellar mass of a galaxy ($M_\star$) is linearly proportional to the host dark matter halo mass $M_{\rm halo}$, i.e. $M_\star = f_\star \left(\frac{\Omega_B}{\Omega_m}\right) M_{\rm halo}$. The quantity $f_\star$ is the fraction of baryons residing in stars within a galaxy. We fix $f_\star = 0.02$ in this study (Behroozi & Silk 2015; Sun & Furlanetto 2016). GRIZZLY also uses a galaxy spectral energy distribution (SED) per stellar mass in the 1D radiative transfer step. The galaxy SED per stellar mass is generated for standard star-formation scenarios using the code PEGASE2[10] (Fioc & Rocca-Volmerange 1997). The initial mass function (IMF) of the stars, within the mass range 1–100 $M_\odot$ in the galaxies, is assumed as a Salpeter IMF and the galaxy metallicity is assumed to be 0.1 $Z_\odot$ throughout the EoR. The emission rate of ionizing photons per unit stellar mass $\dot{N}_i$ from a halo is controlled by the ionization efficiency (ζ) parameter used in GRIZZLY. $\dot{N}_i = \zeta \times 2.85 \times 10^{45}$ s^{-1} $M_\odot^{-1}$ where $\zeta = 1$ corresponds to $\dot{N}_i$ of PEGASE2 SED per stellar mass. We fix $\zeta = 0.1$ for all the reionization models considered in this study. This results in EoR ending around $z \approx 6.5$. On the other hand, the emission rate of X-ray photons per unit stellar mass $\dot{N}_X$ from a halo is controlled by X-ray heating efficiency parameter f_X, where $\dot{N}_X = f_X \times 10^{42}$ s^{-1} $M_\odot^{-1}$. The value of $\dot{N}_X$ for $f_X = 1$ is consistent with the measurements of 0.5–8 keV band high mass X-ray binary SEDs in local star-forming galaxies (Mineo, Gilfanov & Sunyaev 2012). The X-ray SED of the source is modelled using a power law of energy E as $I_X(E) \propto E^{-\alpha}$. We fix the spectral index $\alpha = 1.2$ throughout the work (Berk et al. 2001; Vignali, Brandt & Schneider 2003). The X-ray band here spans from 0.1 to 10 keV. We vary f_X parameters to model different heating (or CD) scenarios of the IGM. The details of the SEDs can be found in Ghara et al. (2015a) and Islam et al. (2019).

Subsequently, we create a library of a large number of 1D profiles of hydrogen ionization fraction $x_{\rm H\,II}$, and gas temperature T_K around isolated sources for different combinations of stellar masses, redshifts, and density contrast. We use these profiles to generate coeval cubes of neutral fraction $x_{\rm H\,I}$ and T_K at different redshifts. The 21-cm signal strength also crucially depends on the Ly-α photons flux. The Ly-α flux maps are generated assuming a $1/R^2$ decrease of the Ly-α photons flux with radial distance R from the source. We refer the readers to Ghara et al. (2015a) and Islam et al. (2019) for more details about these calculations. The T_K cubes and the Ly-α flux maps are used to generate the spin temperature T_s maps assuming that the collisional coupling is negligible at the concerned redshifts. These $x_{\rm H\,I}$, T_s cubes and the density fields are then used to generate the brightness temperature maps of the 21-cm signal (see e.g. Madau, Meiksin & Rees 1997; Furlanetto, Peng Oh & Briggs 2006):

$$\delta T_b(\boldsymbol{n}, \nu) = 27\, x_{H\,I}(\boldsymbol{n}, z)\,(1 + \delta_B(\boldsymbol{n}, z)) \left(\frac{\Omega_B h^2}{0.023}\right) \times \left(\frac{0.15}{\Omega_m h^2}\frac{1+z}{10}\right)^{1/2} \left(1 - \frac{T_\gamma(z)}{T_s(\boldsymbol{n}, z)}\right) \text{mK}, \quad (1)$$

where $\boldsymbol{n}$ is the position of the observed region in the sky and $\nu = 1420.406/(1 + z)$ MHz is the observation frequency. The CMB brightness temperature is $T_\gamma(z) = 2.725 \times (1 + z)$ K. We then incorporate the effect due to the peculiar velocity of the gas using the cell movement method described by Mao et al. (2012). Finally, we used these coeval cubes of the 21-cm signal brightness temperature to create the LC which accounts for the evolution of the 21-cm signal with redshift. The detailed method to implement the LC effect can be found in Ghara et al. (2015b).

We choose $f_X = 10$ for our fiducial model as it produces heating and reionization peaks in 21-cm 3D power spectra (see Fig. 3) within the redshift range considered here that is comparable to the earlier studies (e.g. Mesinger, Ferrara & Spiegel 2013). The CD for this model starts with a weak signal due to weak Ly-α background around $z \sim 20$ (see the bottom panel of Fig. 1). With the Ly-α coupling becoming efficient at $z \lesssim 13$, X-ray heating dominates the fluctuations of the signal at $9 \lesssim z \lesssim 15$. At $z \lesssim 9$, the signal fluctuation is dominated by ionization fluctuation.

The most important physical processes that determine the strength and fluctuations of the simulated 21-cm signal are the Ly-α coupling, X-ray heating, and the ionization due to UV photons. To study the impact of these processes separately, we consider three different models which are shown in Fig. 1.

(i) Model 1: Considers saturated X-ray heating and Ly-α coupling from the very beginning of the CD (here $z > 20$). In other words, we assume $T_s >> T_\gamma$. Thus, the fluctuations in the signal are determined by the density fluctuations (important during the early stages of reionization) and ionization fluctuations (important during the later stages of reionization). We label this model as 'M1'.

[8]Partnership for advanced computing in Europe: http://www.prace-ri.eu/
[9]http://wiki.cita.utoronto.ca/mediawiki/index.php/CubePM
[10]http://www2.iap.fr/pegase/

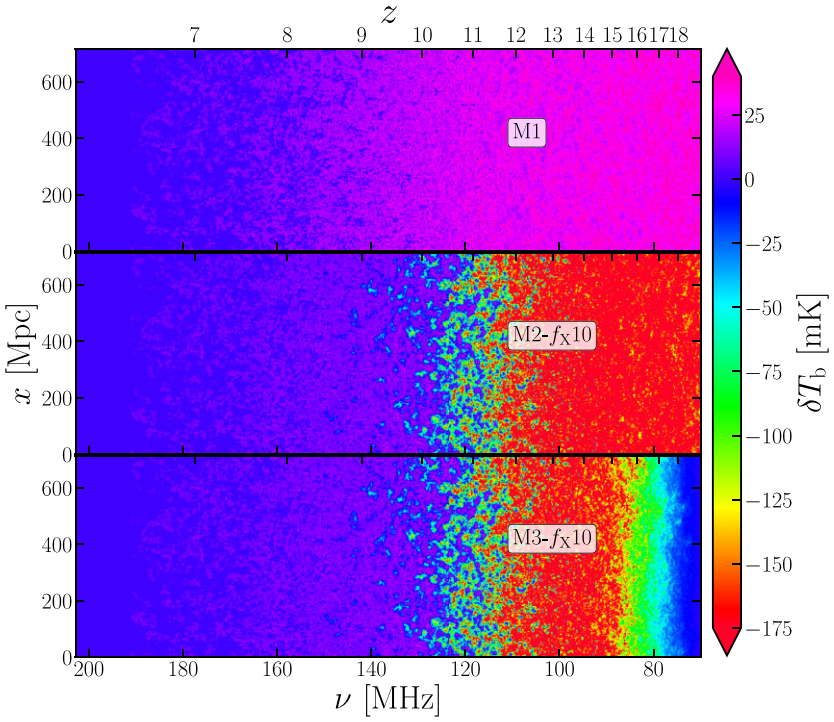

Figure 1. LC slices of simulated CD–EoR 21-cm signal as a function of observing frequency (redshift). The three panels correspond to three different models corresponding to a heating scenario with $f_X = 10$. The details are mentioned in Section 2.1.

(ii) Model 2: Considers X-ray heating self-consistently while assuming the Ly-α coupling is strong from the beginning of the CD. This sets $T_s = T_K$ and δT_b is predominantly governed by matter fluctuations initially. As soon as X-rays start heating the IGM, δT_b starts being governed by the fluctuations in T_s. Thus, we will be able to distinguish the impact of the X-ray heating on the 21-cm MAPS by comparing this model with M1. In this simulation, we set $f_X = 10$. We denote this model by 'M2-f_X10' in our following discussions.

(iii) Model 3: The standard scenario with self-consistent Ly-α coupling and X-ray heating with $f_X = 10$. This is our fiducial model which we denote by 'M3-f_X10'.

We also study the impact of different X-ray heating scenarios on the CD 21-cm MAPS. Thus, for Model 3, we consider two other heating scenarios correspond to $f_X = 1$ (M3-f_X1) and $f_X = 0.1$ (M3-f_X0.1). Fig. 2 shows the LCs of these two heating scenarios in addition to our fiducial model M3-f_X10. As expected, we note that the X-ray heating of IGM is delayed for a smaller value of f_X. In fact, the fraction of emission regions for $f_X = 0.1$ is negligible. Table 1 lists all the different CD source models and X-ray heating scenarios that have been considered in this work.

2.2 LC effect on 3D power spectrum

The 3D power spectrum of the CD–EoR 21-cm signal at any wavenumber $\boldsymbol{k}$ can be written as

$$P(\boldsymbol{k}, z) = V^{-1} \langle \delta\tilde{T}_b(\boldsymbol{k}, z)\, \delta\tilde{T}_b(-\boldsymbol{k}, z) \rangle, \quad (2)$$

where V is the signal volume centred at redshift z and $\langle \cdots \rangle$ denotes an ensemble average. Here $\delta\tilde{T}_b(\boldsymbol{k}, z)$ is the Fourier transformation of the 3D signal $\delta T_b(\boldsymbol{n}, z)$ centred at redshift z which inherently assumes statistical ergodicity and periodicity in the signal volume along all directions. Using equation (2), we estimate 3D power spectrum of the LC 21-cm signal averaged over $\boldsymbol{k}$ modes in logarithmically spaced spherical bins. The solid lines in the top subpanels of Fig. 3 show the dimensionless 3D power spectrum $\Delta^2_b(z) = k^3 P(z)/(2\pi^2)$ computed from the LC boxes shown in Figs 1 and 2. Here, we use a cubical box of volume $V = [500\ h^{-1}\,\mathrm{Mpc}]^3$, centred at desired redshifts (frequency channels) within the LC cube, to obtain $\Delta^2_{b,LC}(k, z)$. We also estimate $\Delta^2_{b,CC}(k, z)$ from coeval cubes of similar volume simulated at redshifts the same as the chosen central redshifts in the LC signal. The evolution of $\Delta^2_{b,LC}$ (solid lines) and $\Delta^2_{b,CC}$ (dashed lines) as a function of z are shown in the top subpanels of Fig. 3 for comparison. We present the results for large ($k = 0.148\ \mathrm{Mpc}^{-1}$) and small ($k = 1.101\ \mathrm{Mpc}^{-1}$) length-scales, respectively, in the left- and right-hand panels. It is important to note that the LC effect tries to flatten the peaks and troughs in the 3D power spectrum due to smoothing as already demonstrated in previous studies (e.g. Datta et al. 2012; Plante et al. 2014; Ghara et al. 2015b; Mondal et al. 2018). The impact of LC effect is more pronounced at smaller k modes since the cosmic evolution becomes important on the large length-scales along LoS. We also plot the percentage deviations in 3D power spectrum due to LC effect, i.e. $\delta_{LC}(\%) = (\Delta^2_{b,CC}/\Delta^2_{b,LC} - 1) \times 100$ per cent.

Considering model M1 (blue lines) in Fig. 3 where X-ray heating is saturated and the signal is driven mainly by the photoionization, we note that the deviation δ_{LC} lies mostly within ± 10 per cent, except between $z = 9.5$ and 12.5 for $k = 0.148\,\mathrm{Mpc}^{-1}$ where δ_{LC} is as large as -60 per cent at $z \approx 11$. Our results for M1 are qualitatively similar to the earlier LC studies of EoR (e.g. Datta et al. 2012, 2014; Plante et al. 2014; Mondal et al. 2018) which demonstrate that the LC effects are important but not as dramatic as we find it. The LC effect is volume-dependent and becomes more(less) pronounced for larger(smaller) volumes. Our choice of such a large volume (≈40 MHz along LoS) is motivated by the future large-bandwidth surveys by *HERA* and *SKA-Low*. The impact of LC effects and δ_{LC} for M3-f_X0.1 (green lines)

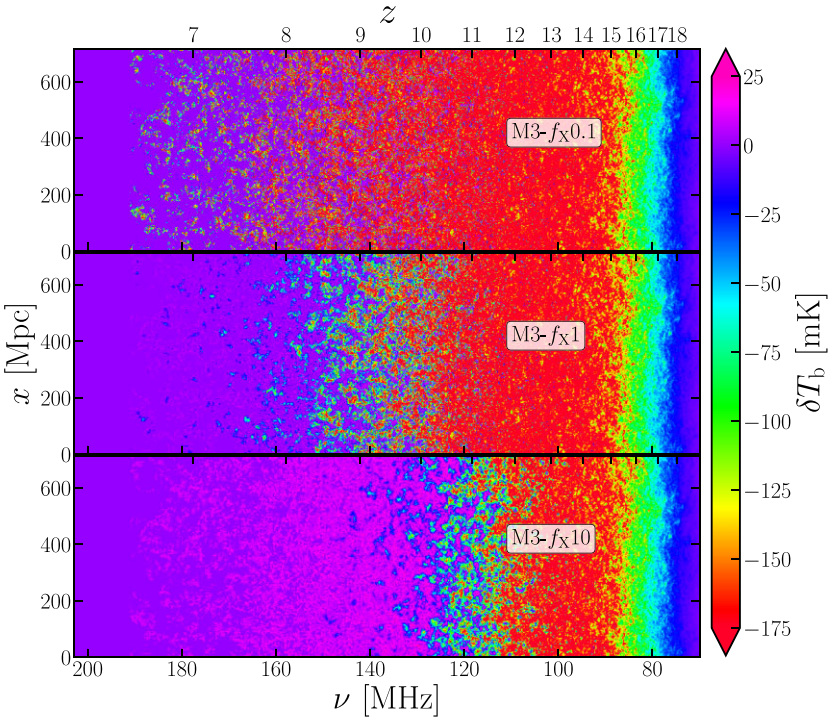

Figure 2. LC slices of simulated CD–EoR 21-cm signal as a function of observing frequency (redshift). The three panels correspond to three different heating scenarios corresponding to model M3. The details are mentioned in Section 2.1.

Table 1. An overview of the different CD–EoR models and heating scenarios considered in this paper.

Models	f_X	T_s	Notations
Model 1	–	$T_s >> T_\gamma$	M1
Model 2	10	$T_s = T_K$	M2-f_X10
Model 3	10	Self-consistent	M3-f_X10
Model 3	1	Self-consistent	M3-f_X1
Model 3	0.1	Self-consistent	M3-f_X0.1

Note. The models above consider all the dark matter haloes with mass larger than 10^9 $M_\odot$ contribute to reionization, heating, and Ly-α coupling. The ionization efficiency parameter ζ is fixed to 0.1. M3-f_X10 is our fiducial simulation.

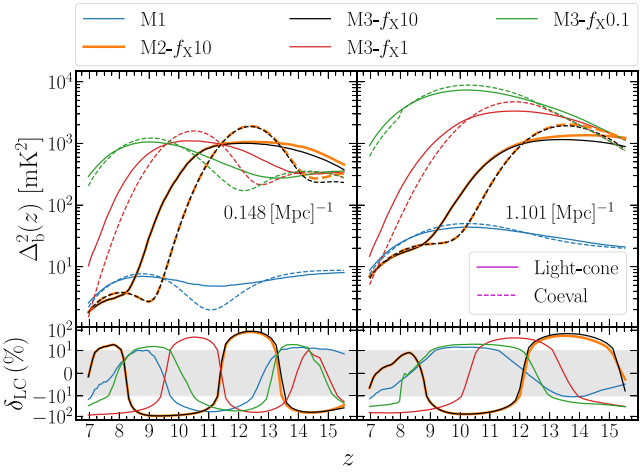

Figure 3. Dimensionless 3D power spectrum $\Delta^2_b(k, z) = k^3 P(k, z)/(2\pi^2)$ computed using LC and coeval signals as a function of redshift (z). Two columns are for two different k modes as written in the panels. Five colours here correspond to the five different simulations (see Table 1). Solid lines in the top subpanels represent 3D power spectra estimated from LC boxes whereas the dashed lines represent those computed using coeval cubes. Solid lines in the bottom subpanels represent percentage deviations in the 3D power spectrum arising due to LC anisotropy. The grey shaded region demarcates the linear scale on the symmetric log axis.

are also similar to M1 as the X-ray heating here is inefficient ($f_X = 0.1$). For the more efficient heating ($f_X = 1$) scenario M3-f_X1, we find that LC effect somewhat enhances δ_{LC}. We find that for M3-f_X1 the clumps of cold H I still remain in the IGM (see Fig. 2) where the 21-cm signal is being controlled by the X-ray heating, this allows the deviations to remain important up to $z = 7$. The dramatic effect of LC anisotropy on $\Delta^2_b(z)$ due to X-ray heating is clearly seen for M2-f_X10 (orange lines) and M3-f_X10 (black lines) where $f_X = 10$. We note that the distinct X-ray peak in coeval $\Delta^2_b(z)$ (dashed lines) is completely flattened due to LC smoothing. Additionally, a peak appears in the coeval $\Delta^2_b(z)$ during the initial stages of the CD ($z \gtrsim 18$) due to fluctuations arising from unsaturated Ly-α coupling. This peak can also get smoothed out in the LC 3D power spectrum. However, we could not compute the LC 3D power spectrum (3DPS) due to the limited redshift range of the available LC cube, and thus the peak is not shown in Fig. 3. The deviations here are varying roughly within a range of −95 per cent to +88 per cent and the large deviations are limited to CD and very initial phase of EoR. The LC effect dies down as soon as IGM temperature gets saturated over T_γ ($z < 8$). Note that, our calculations of the 3DPS also include the pure LoS k modes as well, i.e. when $\boldsymbol{k}_\perp = 0$, which is not the case in real observations where $\boldsymbol{k}_\perp = 0$ modes are absent. Therefore, the deviations reported above represents a ceiling for the δ_{LC}(per cent) expected from the observations. However, removing $\boldsymbol{k}_\perp = 0$ from our analysis does not change the final conclusions and they qualitatively agree with the

previous study by Ghara et al. (2015b) which concludes that the LC effects cannot be ignored for the 21-cm signal during CD.

2.3 Multifrequency angular power spectrum

This work aims to quantify the CD–EoR 21-cm signal using power spectrum statistics while considering the inevitable LC effect that makes the signal non-ergodic and aperiodic along the LoS direction. The 3D Fourier modes $\boldsymbol{k}$, therefore, will be an inappropriate choice of basis and the widely used 3D power spectrum $\Delta^2_{\rm b}(\boldsymbol{k}, z)$ will provide biased estimates of the signal $\delta T_{\rm b}(\boldsymbol{n}, \nu)$. This restricts utility of the 3D power spectrum estimator in analysing data in chunks of small bandwidths, thereby limiting access to the large-scale modes along the LoS axis. Moreover, the inference pipelines which compare the 3D power spectra computed from the observed data and coeval 21-cm signal simulations are expected to bias the resultant parameters. In order to claim a fair comparison between simulations and observations, one can properly incorporate the LC effect in inference pipelines. Intuitively one can claim that this approach will avoid the bias in the parameters. However, including the LC effects in the modelling does not rectify the fact that the 3D power spectrum assumes ergodicity along the LoS axis. Thus, the 3D power spectrum is still the incorrect basis for parameter exploration and can still bias the inferred parameter values. One needs to check these claims for the CD–EoR 21-cm signal. The MAPS is a non-stationary two-point statistics which is a suitable alternative for the 3D power spectrum. MAPS, which by definition relaxes the assumption of statistical homogeneity and periodicity along the LoS axis, can completely quantify the two-point statistics of the CD–EoR 21-cm signal observed across a large-frequency bandwidth. In general, MAPS is defined by correlating the amplitudes of the orthonormal spherical harmonics $Y^{\rm m}_{\ell}(\boldsymbol{n})$ at different observing frequencies (redshifts), after decomposing the signal in a spherical basis set (see equation 4 of Mondal et al. 2020a) defined on the spherical sky-surfaces corresponding to these frequencies. This decomposition only assumes the signal to be statistically homogeneous and periodic on the spherical sky-surface.

This study further considers the signal to be coming from a small patch in the sky which allows us to work in flat-sky regime where the CD–EoR 21-cm signal can be represented by $\delta T_{\rm b}(\boldsymbol{\theta}, \nu)$ with $\boldsymbol{\theta}$ being 2D vector on the flat-sky plane. Here, we use the 2D Fourier transform $\delta \tilde{T}_{\rm b2}(\boldsymbol{U}, \nu)$ of the signal $\delta T_{\rm b}(\boldsymbol{\theta}, \nu)$, where $\boldsymbol{U}$ (also known as baseline vector) is the Fourier conjugate of $\boldsymbol{\theta}$. We can also write $\boldsymbol{U} = \boldsymbol{k}_{\perp}/r_{\nu}$ under the flat-sky assumption, where $\boldsymbol{k}_{\perp}$ is the component of $\boldsymbol{k}$ perpendicular to the LoS direction and r_{ν} is the comoving distance to the observing frequency. $\delta \tilde{T}_{\rm b2}(\boldsymbol{U}, \nu)$ is the primary observed entity of the radio-interferometric observations which can be directly used to compute MAPS without any further processing of the observed signal. Using the flat sky approximation, we can define MAPS as

$$\mathcal{C}_{\ell}(\nu_1, \nu_2) = \Omega^{-1} \langle \delta \tilde{T}_{\rm b2}(\boldsymbol{U}, \nu_1) \delta \tilde{T}_{\rm b2}(-\boldsymbol{U}, \nu_2) \rangle, \tag{3}$$

where $\ell = 2\pi |\boldsymbol{U}|$ and Ω is the solid angle subtended by the observed (or simulated) sky-patch to the observer. Note that the statistical ergodicity on the sky-patch allows the signal to correlate only at the same baselines $\boldsymbol{U}$. MAPS does not lose any two-point information if the CD–EoR signal is statistically isotropic on the sky plane. If the signal $\delta T_{\rm b}(\boldsymbol{\theta}, \nu)$ were statistically homogeneous and periodic along the LoS axis, then equation (3) would have been a function of distance separation along the LoS axis instead of ν_1 and ν_2 separately.

Considering a LC box with typically $\sim 300 \times 300 \times 900$ voxels, it will be computationally intractable to store MAPS estimates at each and every combination of cells. Also individual estimates will be too noisy due to statistical fluctuations. In order to circumvent these issues, we compute binned-averaged MAPS by averaging over estimates within a circular bin on ℓ plane. We define the binned MAPS estimator for any ith bin as

$$\hat{\mathcal{C}}_{\ell_i}(\nu_1, \nu_2) = \frac{1}{2\Omega} \sum_{\boldsymbol{U}_{{\rm g}_i}} w_{{\rm g}_i} [\delta \tilde{T}_{\rm b2}(\boldsymbol{U}_{{\rm g}_i}, \nu_1) \delta \tilde{T}_{\rm b2}(-\boldsymbol{U}_{{\rm g}_i}, \nu_2) + \delta \tilde{T}_{\rm b2}(\boldsymbol{U}_{{\rm g}_i}, \nu_2) \delta \tilde{T}_{\rm b2}(-\boldsymbol{U}_{{\rm g}_i}, \nu_1)], \tag{4}$$

where the summation is over all the cells $\boldsymbol{U}_{{\rm g}_i}$ in the ith bin and $w_{{\rm g}_i} \equiv w(\boldsymbol{U}_{{\rm g}_i})$ denotes the weight corresponding to each cell. The two terms on the right-hand side of equation (4) and the factor 1/2 appear because of the symmetry $\mathcal{C}_{\ell}(\nu_1, \nu_2) = \mathcal{C}_{\ell}(\nu_2, \nu_1)$. Also note that the weight $w_{{\rm g}_i}$, in general, can be a function of the two frequencies (ν_1, ν_2) as well. In order to compute the bin-averaged MAPS $\bar{\mathcal{C}}_{\ell}(\nu_1, \nu_2)$, we should perform ensemble average of equation (4), i.e. $\bar{\mathcal{C}}_{\ell_i}(\nu_1, \nu_2) \equiv \langle \hat{\mathcal{C}}_{\ell_i}(\nu_1, \nu_2) \rangle$. However, in this work, we only have single realization of the 21-cm signal which we use to compute $\bar{\mathcal{C}}_{\ell_i}(\nu_1, \nu_2)$.

In this work, we use a modified version of the publicly available MAPS code[11] which has been used in previous works (Mondal, Bharadwaj & Datta 2018; Mondal et al. 2019, 2020a). We now motivate and describe the modifications implemented in the existing code. The LC boxes, mentioned in Section 2.1, are created by stacking the slices of similar dimensions (in the transverse plane) from the coeval boxes. The LC boxes, thus created, subtend different solid angles at the observer in different channels for being located at a different LoS distances. The nearest slice subtends the largest solid angle and *vice-versa*. Similarly, the size of each cell on different slices will be scaled accordingly as the number of cells per slice is fixed. This, in turn, produces baseline planes whose extent $U_{\rm max}$ and the cell size ΔU will vary along the frequency axis. The current available version of code ignores the variation in LoS comoving distance across the frequency band of the LC boxes. It considers only one comoving distance, corresponding to the central frequency of the LC box, while performing the 2D Fourier transform to obtain $\delta \tilde{T}_{\rm b2}(\boldsymbol{U}_{\rm g}, \nu)$ from $\delta T_{\rm b}(\boldsymbol{\theta}, \nu)$. Afterwards, it correlates $\delta \tilde{T}_{\rm b2}(\boldsymbol{U}_{\rm g}, \nu)$ at the same cells in different frequency channels to compute $\mathcal{C}_{\ell}(\nu_1, \nu_2)$. This approximation is fair only when the frequency difference $|\nu_1 - \nu_2|$ is sufficiently small (e.g. Mondal et al. 2019, 2020a). In general, the value $\boldsymbol{U}_{{\rm g}_i}$ corresponding to any particular ith cell will be different for two different frequency channels and therefore the correlation will not provide the estimate of MAPS.

We have modified the existing version of code to resolve this issue by properly treating the variation in LoS distance across the frequency bandwidth of our simulations. The modifications can be listed under the following points.

(i) We first perform 2D Fourier transforms for every slice to obtain $\delta \tilde{T}_{\rm b2}(\boldsymbol{U}_{\rm g}, \nu)$ at the respective frequency channel.

(ii) We next define a common gridded *uv* plane whose extent and the cell size remains uniform across different frequency channels. In this case, the extent $U_{\rm max}$ is set by the maximum baseline cell of the nearest slice (smallest redshift) of the LC box as it is the least. The maximum values of the baseline cells increases with the LoS distance. We also fix the cell size of this common *uv* plane to be the same as that of the farthest frequency slice which is the largest cell size among all frequency channels.

(iii) We now interpolate $\delta \tilde{T}_{\rm b2}(\boldsymbol{U}_{\rm g}, \nu)$ from the frequency varying *uv* planes to the common *uv* plane following the nearest cell method.

[11] https://github.com/rajeshmondal18/MAPS

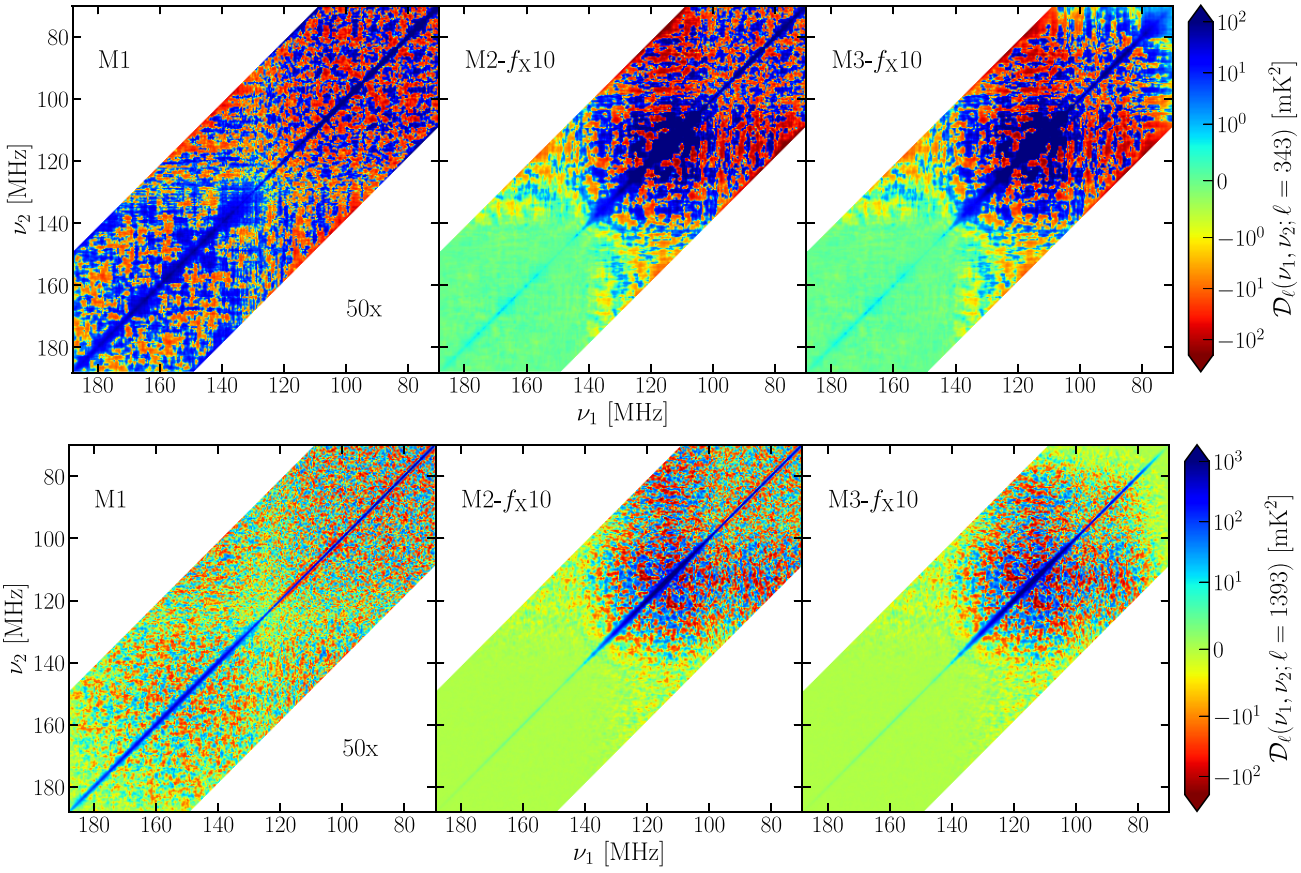

Figure 4. The scaled MAPS $\mathcal{D}_\ell(\nu_1, \nu_2) = \ell(\ell+1)\mathcal{C}_\ell(\nu_1, \nu_2)/(2\pi)$ for different CD–EoR models. The three columns here correspond to models M1, M2-$f_{\rm X}10$, and M3-$f_{\rm X}10$, whereas the two rows correspond to the different ℓ bins as labelled in the colour bar. We scale the MAPS values for M1 by a factor of 50 to make the patterns visible in the same colour bar.

(iv) Finally we correlate the interpolated $\delta\tilde{T}_{\rm b2}(\boldsymbol{U}_{\rm g}, \nu)$ on the cells of the common uv planes across the frequency channels to estimate $\mathcal{C}_\ell(\nu_1, \nu_2)$.

Note that all the results shown in the following sections have been estimated following the modifications listed above.

3 ASTROPHYSICAL IMPLICATIONS

We compute $\bar{\mathcal{C}}_{\ell_i}(\nu_1, \nu_2)$ for the LC boxes simulated using methodology described in Section 2.3. Here, we consider the accessible $\boldsymbol{\ell}$-plane by dividing it into 10 log-spaced circular bins, for which we compute the bin-averaged MAPS (equation 4). Note that we do not perform additional binning of our MAPS estimator along the frequency axis in this paper to retain the evolution information of the signal. However, one can always do channel averaging to reduce the noise in the estimates at the cost of smearing out small-scale information along the LoS axis.

3.1 Impact of astrophysical processes

Fig. 4 shows the scaled bin-averaged MAPS $\mathcal{D}_\ell(\nu_1, \nu_2) = \ell(\ell+1)\bar{\mathcal{C}}_\ell(\nu_1, \nu_2)/(2\pi)$ for the three different models (in different columns) considered here (see Fig. 1). The two rows in this figure corresponds to the two ℓ bins having mean values $\ell = 343$ and 1393 which corresponds to, respectively, large (63 arcmin) and intermediate (15.5 arcmin) angular-scales on the sky. Here, we show only a part of the MAPS on (ν_1, ν_2) plane which are within 300 channel grid difference that roughly corresponds to 37 MHz band in frequency. This has to do with the creation of the LC boxes where we simulate signal over ∼900 frequency-grids by repeating slices from the coeval boxes having $[300^3]$ voxels.

We first note that $\mathcal{D}_\ell(\nu_1, \nu_2)$ can have both positive and negative values as the signal from different parts in the observation volume can correlate and anti-correlate. The off-diagonal terms contains the information of the LC evolution of the signal as they are the correlations between different the frequency channels. However, the diagonal MAPS $\mathcal{D}(\nu, \nu)$ is always positive and equivalent to 3DPS estimated on $k_\parallel = 0$ plane. Considering M1 where the IGM is heated well above CMB temperature and $T_{\rm s} >> T_\gamma$, we find from equation (1) that the 21-cm signal $\delta T_{\rm b}$ is governed by the photoionization $x_{\rm HI}$ during EoR and by density fluctuations $\delta_{\rm B}$ during CD. This, in turn, makes the amplitude of contrast in $\delta T_{\rm b}$ (see Fig. 1), and hence the MAPS, small as seen in the panels of Fig. 4. The MAPS estimates in M1 are roughly 50–100 times smaller than the other two models. In contrast with M1, we note that the spin-temperature fluctuations due to unsaturated X-ray heating, introduce larger fluctuations in $\delta T_{\rm b}$ for M2-$f_{\rm X}10$ and M3-$f_{\rm X}10$ (see Fig. 1). This boosts the MAPS for M2-$f_{\rm X}10$ roughly 50–100 times over that in model M1 during the CD. The X-ray heating also makes $\mathcal{D}_\ell(\nu_1, \nu_2)$ positive in a larger region around diagonal $(\nu_1 = \nu_2)$ during the heating epoch, i.e. in the range of 100−130 MHz. This happens because of the heating bubbles which have been grown to a large enough size before the reionization starts. Before the heating ($\nu < 100$ MHz), MAPS for

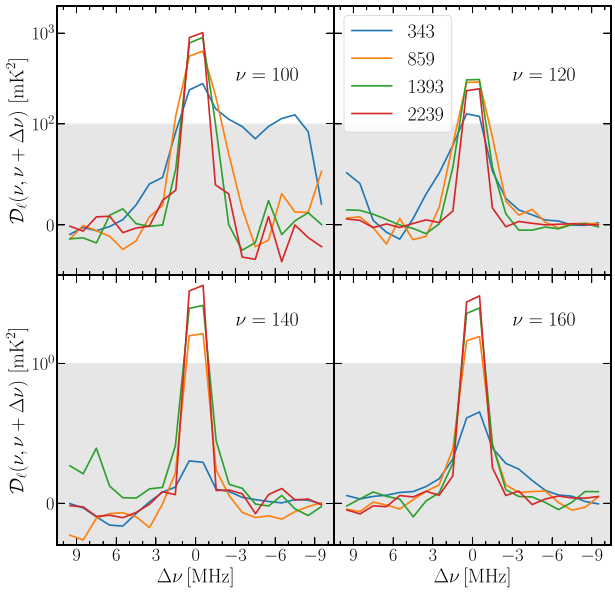

Figure 5. The scaled MAPS $\mathcal{D}_\ell(\nu, \nu + \Delta\nu)$ showing correlations as a function of $\Delta\nu$ for M3-$f_X = 10$. The four different panels corresponds to the frequency channels centred at $\nu = 100$, 120, 140, and 160 MHz. The four different colours in each panel correspond to the four ℓ bins as mentioned in the legend. The grey shades demarcate the linear regime on the symmetric log-scale along vertical axis.

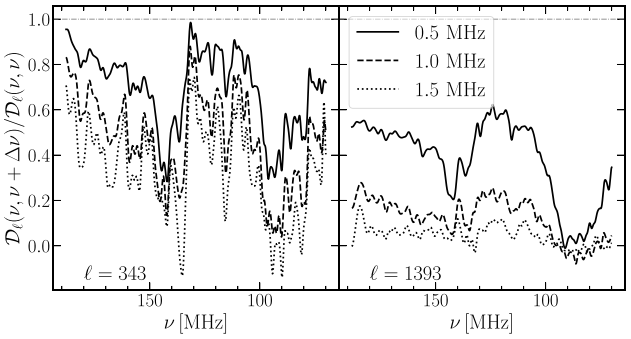

Figure 6. The ratio $\mathcal{D}_\ell(\nu, \nu + \Delta\nu)/\mathcal{D}_\ell(\nu, \nu)$ demonstrating how the correlations between MAPS fall when going off the diagonal as a function of ν for M3-$f_X = 10$. The two different panels correspond to two different ℓ values representing large and intermediate angular-scales on the sky. The three different line styles in each panel correspond to three frequency separations $\Delta\nu = 0.5$, 1.0, and 1.5 MHz. The dot–dashed grey line at the unity represents the case when there is complete correlations.

M1 and M2-f_X10 have similar pattern, however the values are an order of magnitude different. Considering model M3-f_X10, we find the 21-cm MAPS to be the same as that for M2-f_X10 except for the early stages of CD ($\nu < 80$ MHz). This is because the unsaturated Ly-α coupling in M3-f_X10 fails to completely couple T_s to the gas temperature and δT_b starts near to the zero value during the initial stages of CD. This makes the 21-cm signal and its MAPS weaker for M3-f_X10 than in M2-f_X10. The amplitude of the 21-cm signal and thus its MAPS starts decreasing as soon as the X-ray heating puts $T_s >> T_\gamma$ at $\nu \gtrsim 140$ MHz. The signal overall remains positive during EoR (as shown by bluish-green colour) on large-scales (small ℓ) for all the three models considered here. We note that saturated heating of the IGM decreases the 21-cm MAPS by $\sim$2 orders of magnitudes (see Figs 3 and 7) as compared to the CD for both M2-f_X10 and M3-f_X10.

Comparing the top ($\ell = 343$) and the bottom ($\ell = 1393$) rows of Fig. 4, we note that the patterns corresponding to each model are roughly identical on the large and intermediate angular-scales, respectively. We find that for $\ell = 343$, the regions of positive/negative $\mathcal{D}_\ell(\nu_1, \nu_2)$ are extended to larger patches on the frequency plane suggesting that the (anti)correlation between the signal on large-scales does not change rapidly over time. Whereas on small-scales the time-evolution is expected to be faster thereby making the features in $\mathcal{D}_\ell(\nu_1, \nu_2)$ smaller for $\ell = 1393$ on frequency plane. We expect the typical sizes of these contiguous patterns to depend on the different stages of CD–EoR and the physical processes.

Similar to the earlier studies (e.g. Mondal et al. 2020a), we find that the 21-cm MAPS takes larger values along and around the diagonal on the (ν_1, ν_2) plane. $\mathcal{D}(\nu_1, \nu_2)$ decreases rapidly to one order of magnitude or even less, as we move away from diagonal. This is apparent from Fig. 5 which shows $\mathcal{D}(\nu, \nu + \Delta\nu)$ for our fiducial model (M3-f_X10) as a function of $\Delta\nu$ for four different $\nu = 100$, 120, 140, and 160 MHz corresponding to different stages of CD–EoR in four panels. Different coloured lines in each panel correspond to different ℓ values. The rate of decrease at any particular scale (ℓ) depends upon how fast the signal decorrelates with the frequency separation $|\Delta\nu|$ which in turn depends upon the progression-speed of the underlying physical processes governing the signal in the IGM. We note that the rate at which the signal decorrelates with increasing $|\Delta\nu|$ is slower for smaller ℓ values and *vice-versa*. We expect the behaviour of $\mathcal{D}(\nu, \nu + \Delta\nu)$ to be asymmetrical around $\Delta\nu = 0$ as the astrophysical processes may not behave symmetrically around any reference frequency ν. This asymmetry can be more prominent for large-angular scales as can be seen for $\ell = 343$ here. The level of asymmetry in the curves will again be dependent on how fast the physical processes evolve the signal at the concerned instant of time. In Fig. 6, we show the ratio $\mathcal{D}(\nu, \nu + \Delta\nu)/\mathcal{D}(\nu, \nu)$ as a function of ν for three different values of $\Delta\nu = 0.5$, 1.0, and 1.5 MHz using solid, dashed, and dotted lines, respectively. Here, we can clearly see the signal decorrelates at a slower rate wherever X-ray heating determines the 21-cm signal (i.e. $\nu \approx 100$–140 MHz) for both the ℓ values. The decorrelation of the signal is faster during the beginning of CD and the EoR. Therefore, we conclude that a large amount of information of the signal is encoded in the diagonal element of $\mathcal{D}(\nu_1, \nu_2)$. However, in principle, one can also exploit the off-diagonal terms (at least near around the diagonal) while interpreting the signal especially when the X-ray heating is crucial.

Fig. 7 shows the diagonal term $\mathcal{D}_\ell(\nu, \nu)$ against four bins centred at $\ell = 343$, 859, 1393, and 2239 for the three models M1, M2-f_X10, and M3-f_X10. We find that the qualitative behaviour is similar to the coeval 3DPS (Fig. 3). This clearly indicates, while analysing a large-bandwidth signal, MAPS shows the evolutionary features more distinctly than the spherically averaged 3DPS. However, this comparison is not so straightforward and fair. The advantage of MAPS over 3DPS completely depends on the way we bin and analyse the data. For example, computing the 3DPS by dividing the data into chunks of smaller bandwidths can perform better than when analysing it in a larger bandwidth. Although, it does not change the fact that there will be LC bias in the estimates due to LoS Fourier transformation. As expected, $\mathcal{D}_\ell(\nu, \nu)$ is smaller for M1 due to aforementioned reasons. We note that the 21-cm MAPS first decreases as the redshift decreases (or frequency increases). This shallow decrease is because the ionizing radiation wipes out H I residing only in the high-density peaks (small-scales) during

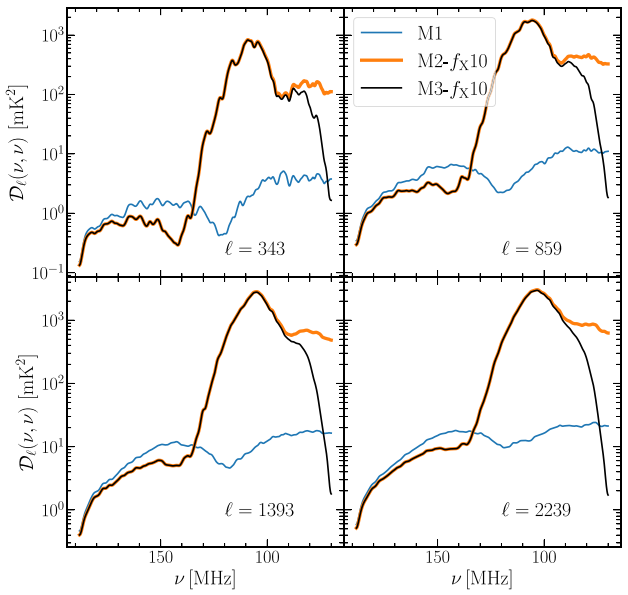

Figure 7. Diagonal of the scaled MAPS $\mathcal{D}_\ell(\nu,\nu) = \ell(\ell+1)\mathcal{C}_\ell(\nu,\nu)/(2\pi)$ as a function of ν. The four panels corresponds to the four different ℓ bins as labelled. The three colours in each panel refer to the three models M1, M2-f_X10, and M3-f_X10 as shown in the legend.

the initial stages. However, as the reionization progresses further (towards higher frequencies), the fluctuations due to ionized and neutral regions starts increasing the 21-cm MAPS after the first dip at $\nu = 120$ MHz as seen in the figure. $\mathcal{D}_\ell(\nu,\nu)$ reaches its maximum when the universe is 50 per cent ionized around $\nu = 140-150$ MHz. The 21-cm MAPS drops again towards the larger frequencies as the reionization proceeds to the end. Considering models M2-f_X10 and M3-f_X10, the unsaturated heating during CD ($\nu \lesssim 130$ MHz) introduces large fluctuations in spin-temperature T_s and thereby in the signal. This causes the 21-cm MAPS to increase upto two orders of magnitude in CD regime, when compared with M1. The 21-cm MAPS peaks at $\nu \approx 110$ MHz at all the angular-scales shown here in the four panels. M2-f_X10 and M3-f_X10 are nearly identical except for the very initial stages, i.e. $\nu < 90$ MHz. In M3-f_X10, the Ly-α coupling is not saturated from the beginning, and thus T_s starts at a temperature near to T_γ resulting into small amplitude of fluctuations and consequently smaller values of 21-cm MAPS. As the IGM evolves (towards higher frequencies), the Ly-α photons couple T_s to matter temperature and therefore the amplitude of the 21-cm signal and its MAPS shows a rise in M3-f_X10. However, in M2-f_X10 the Ly-α coupling is saturated, allowing $T_s \approx T_K$ from the beginning, and therefore the 21-cm MAPS is dominated by the matter fluctuations and remains almost constant till a point ($\nu \approx 90$ MHz) where the X-ray heating starts playing important role in modulating T_s.

Note that we have chosen $f_X = 10$ for simulating the 21-cm signal for M2-f_X10 and M3-f_X10. However, to simulate the signal for M1, where the heating of IGM is saturated from the beginning of the CD ($\nu = 70$ MHz), we need to choose a larger value for f_X. Therefore, the heating in M2-f_X10 and M3-f_X10 are comparatively delayed due to which the dip before EoR is occurring at a later redshift (larger frequency) than M1. Late heating is also the reason for the mismatch in the value of $\mathcal{D}_\ell(\nu,\nu)$ during the initial and middle stages ($\nu \sim 150$ MHz) of reionization. However towards the end of the reionization the heating of IGM is saturated as expected, which in turn causes the MAPS for all the three models to converge. Note that we treat M3-f_X10 as our fiducial model in the rest of this work as this model is closer to realistic scenario based on current theoretical understanding.

3.2 Impact of X-ray heating efficiencies

We further study the effects of different heating efficiencies $f_X = 0.1$, 1, and 10 on 21-cm MAPS for our fiducial model M3. The signal for the three scenarios is expected to be similar until X-ray heating starts playing important role in modulating T_s. This behaviour is apparent from Fig. 8 which shows $\mathcal{D}_\ell(\nu_1,\nu_2)$ for M3-f_X0.1, M3-f_X1, and M3-f_X10. We clearly see that pattern on the (ν_1,ν_2) plane is qualitatively similar for all the three scenarios as long as the Ly-α coupling plays important role. We also note that the 21-cm MAPS becomes strictly positive over a large region near the diagonal ($\nu_1 \approx \nu_2$) once the X-ray heating or the ionizing photons starts becoming important for the signal. The frequency at which this happens decreases with the increase in f_X value. Also, the IGM gets heated to a saturation level quickly for larger f_X values and the 21-cm MAPS decreases at a faster rate towards larger frequencies (lower redshifts) as seen in Figs 8 and 9.

We plot the diagonal MAPS $\mathcal{D}_\ell(\nu,\nu)$ in Fig. 9, where the four panels again corresponds to the four bins centred at $\ell = 343$, 859, 1393, and 2239. Considering M3-f_X0.1, we find that the heating of the IGM is inefficient here and we still find cold H I clouds till the end of the EoR (see top panel of Fig. 2). For this reason the heating peak is absent in this scenario. The second peak (at larger frequency) here is due to the reionization. The behaviour of 21-cm MAPS here is qualitatively similar to that in M1 except for its values which are orders of magnitude larger. We find the heating peak of 21-cm MAPS exists for both M3-f_X1 and M3-f_X10. However, the peak for M3-f_X1 occurs at a later redshift (larger frequency) than that in M3-f_X10. We also note that the reionization peak in 21-cm MAPS is absent for M3-f_X1 as the IGM was not heated sufficiently for the signal to get governed majorly by the ionization field. This is not the case for M3-f_X10, for which the heating of IGM gets saturated before the reionization starts and we do see a reionization peak in this scenario. The dependence of the CD–EoR 21-cm MAPS on heating efficiencies is qualitatively similar to what have been observed in the 3D power spectra computed from the coeval boxes of CD–EoR 21-cm signal in previous studies (e.g. Mesinger et al. 2013; Ghara et al. 2015a; Shimabukuro et al. 2015).

4 DETECTABILITY

At first, we derive the formula for the error covariance of the MAPS statistics here. Later, we use the formula to predict the detectability of the diagonal component of the CD–EoR 21-cm MAPS, i.e. $\mathcal{D}_\ell(\nu,\nu)$, in the context of observations using *HERA*, *NenuFAR*, and the upcoming *SKA-Low*.

4.1 MAPS error covariance

Any radio-interferometer directly measures the CD–EoR 21-cm signal visibilities $\delta\tilde{T}_{b2}(\boldsymbol{U},\nu)$ at frequency, say, ν and baselines $\boldsymbol{U} = \boldsymbol{d}/\lambda$, where $\boldsymbol{d}$ is the antenna-pair separation projected onto the sky-plane, perpendicular to a chosen central LoS, and λ is the wavelength corresponding to ν. The baseline tracks in different frequency channels are the points where the incoming signal is being sampled. The system noise, which originates from statistical fluctuations in the sky and the receivers, is inherent to any radio-interferometric measurement. Additionally, the foreground and other systematic errors corrupt the actual cosmological signal. This contamination

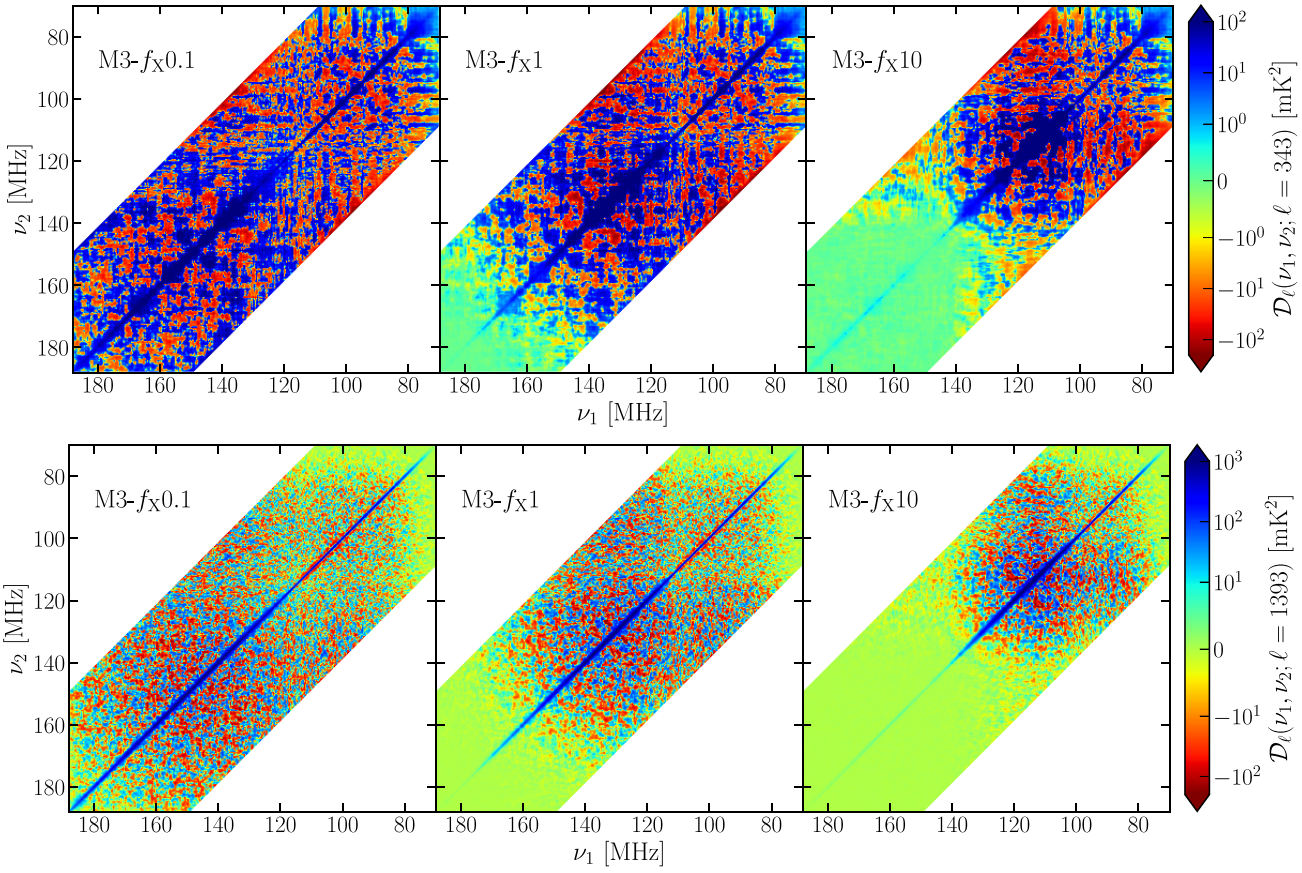

Figure 8. The scaled MAPS $\mathcal{D}_\ell(\nu_1, \nu_2) = \ell(\ell+1)\mathcal{C}_\ell(\nu_1, \nu_2)/(2\pi)$ for different heating scenarios. The three columns here are for three heating efficiencies $f_X = 0.1,\ 1$, and 10 corresponding to the self-consistent model M3. The two rows correspond to the different ℓ bins as labelled in the colour bar.

affects the MAPS estimate as well as the corresponding error in the measurement. However, in this analysis, we assume that the foreground is perfectly modelled and completely removed from the data and also that systematic errors have been removed. Therefore, the measured visibilities will be the sum of cosmological 21-cm signal and the system noise, i.e. $\tilde{T}_{t2}(\boldsymbol{U}, \nu) = \delta\tilde{T}_{b2}(\boldsymbol{U}, \nu) + \tilde{T}_{N2}(\boldsymbol{U}, \nu)$. The system noise is a Gaussian random field on sky-surface and hence $\tilde{T}_{N2}(\boldsymbol{U}, \nu)$ can be assumed to be uncorrelated at different baselines and frequencies. Therefore according to equation (3), the MAPS of the total observed signal will then be the sum of signal MAPS $\mathcal{C}_\ell(\nu_1, \nu_2)$ and the system noise MAPS $\mathcal{C}^N_\ell(\nu_1, \nu_2)$, i.e. $\mathcal{C}^t_\ell(\nu_1, \nu_2) = \mathcal{C}_\ell(\nu_1, \nu_2) + \delta^K_{\nu_1,\nu_2}\mathcal{C}^N_\ell(\nu_1, \nu_2)$. The Kroneker's delta $\delta^K_{\nu_1,\nu_2}$ appears here due to the fact that the Gaussian system noise at different frequencies remains uncorrelated. Although it is possible to remove the noise bias from the total MAPS estimate (Bharadwaj et al. 2018), its contribution to the total measurement error still remains.

Ignoring the non-Gaussianity of the underlying 21-cm field, we have calculated the error covariance matrix of the bin-averaged MAPS estimator (equation 4) which, in general, can be written as (see appendix A of Mondal et al. 2020a, for the derivation)

$$\begin{aligned} \boldsymbol{X}^{\ell_i}_{12,34} &= \langle \delta\hat{\mathcal{C}}^t_{\ell_i}(\nu_1, \nu_2)\, \delta\hat{\mathcal{C}}^t_{\ell_i}(\nu_3, \nu_4)\rangle \\ &= \frac{1}{2}\sum_{\boldsymbol{U}_{g_i}} w^2_{g_i}\Big[\mathcal{C}^t_{\ell_{g_i}}(\nu_1, \nu_3)\mathcal{C}^t_{\ell_{g_i}}(\nu_2, \nu_4) \\ &\quad + \mathcal{C}^t_{\ell_{g_i}}(\nu_1, \nu_4)\mathcal{C}^t_{\ell_{g_i}}(\nu_2, \nu_3)\Big]\ , \end{aligned} \tag{5}$$

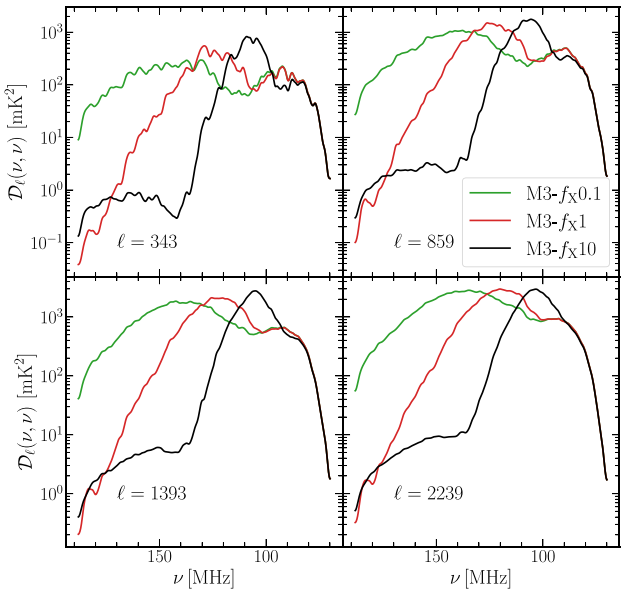

Figure 9. Diagonal of the scaled MAPS $\mathcal{D}_\ell(\nu, \nu) = \ell(\ell+1)\mathcal{C}_\ell(\nu, \nu)/(2\pi)$ as a function of ν. The four panels correspond to the four different ℓ bins as labelled. The three colours in each panel are for three heating efficiencies $f_X = 0.1,\ 1$, and 10 corresponding to model M3.

Table 2. Observational parameters for different radio-interferometers used to compute the system noise MAPS $\mathcal{C}_{\ell}^{\rm N}(\nu,\nu)$ in this analysis.

Telescopes	No. of stations	Diameter (m)	Frequency bandwidth (MHz)	Channel width (kHz)	$T_{\rm rec}$ (K)	Pointing direction	$\ell_{\rm max}$	$\Delta\ell$	Survey mode
HERA	350	14	50–250	97.66	170	$-30^\circ43'17''$	11 250	97.82	Drift scan
NenuFAR	102	25	10–85	195.32	1000	$+47^\circ22'34''$	12 093	108.95	Field track
SKA-Low	512	35	50–350	97.66	100	$-26^\circ49'29''$	11 250	97.82	Field track

Note. Here, $T_{\rm rec}$ denotes the antenna receiver temperature in K. $\ell_{\rm max}$ denotes the maximum extent of the square ℓ plane from its centre and $\Delta\ell$ denotes the corresponding cell size, considered for the noise predictions. Note that we consider observations per night to be of 8 h.

where $\delta\hat{\mathcal{C}}^{\rm t}_{\ell_i}$ denotes the deviation of $\hat{\mathcal{C}}^{\rm t}_{\ell_i}$ from its ensemble mean and $w_{\rm g_i}$ is the weight corresponding to each cell and the summation is over the cells $\boldsymbol{U}_{\rm g_i}$ within the ith bin. It is apparent from equation (5) that the errors in different baseline cells $\boldsymbol{U}_{\rm g}$ are completely uncorrelated here. This is because of our Gaussian assumption for both the signal and the system noise field. However, the errors may be correlated for two different pairs of frequencies, i.e. (ν_1,ν_2) and (ν_3,ν_4). In reality, the CD–EoR 21-cm signal is a non-Gaussian field (e.g. Bharadwaj & Pandey 2005; Harker et al. 2009) due to non-Gaussianity arising due to various factors such as $x_{\rm HI}$, $\delta_{\rm B}$, $T_{\rm s}$ in the signal (equation 1). This non-Gaussianity gives rise to the non-zero contributions from angular trispectrum to the cosmic variance (CV) of MAPS and also introduces correlations between different baselines (e.g. Mondal et al. 2015; Mondal, Bharadwaj & Majumdar 2016). Mondal et al. (2016) and Mondal, Bharadwaj & Majumdar (2017) have developed a novel technique to estimate the 3D trispectrum from a moderately large ensemble of 21-cm simulations. One can extend their technique to estimate the angular trispectrum for the CD–EoR 21-cm signal, although it will be more computationally challenging. Hence, we drop the non-Gaussian contribution in our calculations and analysis. Recently, Shaw et al. (2019) have studied the importance of trispectrum contribution to the total error prediction in 3D power spectrum in the context of future *SKA-Low* observations. Following their results, we argue that non-Gaussian effects will be important for the small and intermediate ℓ bins where the system noise contribution is relatively smaller.

Here, we simplify the full error covariance matrix and restrict ourselves to predicting the error variance of our MAPS estimator which can be written as

$$\begin{aligned}\boldsymbol{X}^{\ell_i}_{12,12} &= [\boldsymbol{\sigma}^{\ell_i}_{12}]^2 = \langle[\delta\hat{\mathcal{C}}^{\rm t}_{\ell_i}(\nu_1,\nu_2)]^2\rangle \\ &= \frac{1}{2}\sum_{\boldsymbol{U}_{\rm g_i}} w^2_{\rm g_i}\left[\mathcal{C}^{\rm t}_{\ell_{\rm g_i}}(\nu_1,\nu_1)\mathcal{C}^{\rm t}_{\ell_{\rm g_i}}(\nu_2,\nu_2)+\{\mathcal{C}^{\rm t}_{\ell_{\rm g_i}}(\nu_1,\nu_2)\}^2\right] \\ &= \frac{1}{2}\sum_{\boldsymbol{U}_{\rm g_i}} w^2_{\rm g_i}\Big[\{\mathcal{C}_{\ell_{\rm g_i}}(\nu_1,\nu_1)+\mathcal{C}^{\rm N}_{\ell_{\rm g_i}}(\nu_1,\nu_1)\} \\ &\quad\times\{\mathcal{C}_{\ell_{\rm g_i}}(\nu_2,\nu_2)+\mathcal{C}^{\rm N}_{\ell_{\rm g_i}}(\nu_2,\nu_2)\} \\ &\quad+\{\mathcal{C}_{\ell_{\rm g_i}}(\nu_1,\nu_2)+\delta^{\rm K}_{\nu_1,\nu_2}\mathcal{C}^{\rm N}_{\ell_{\rm g_i}}(\nu_1,\nu_2)\}^2\Big]. \end{aligned} \tag{6}$$

Hence, we need the weights $w_{\rm g}$, the 21-cm MAPS $\mathcal{C}_{\ell_{\rm g}}(\nu_1,\nu_2)$, and the system noise MAPS $\mathcal{C}^{\rm N}_{\ell_{\rm g}}(\nu_1,\nu_2)$ at every $\boldsymbol{\ell}_{\rm g}$ cell to predict the error variance in 21-cm MAPS. We have estimated the 21-cm bin-averaged MAPS using simulated signal LC boxes. Note that the bin-averaged MAPS presented above in Section 3 considers uniform weights across the cells while estimating $\bar{\mathcal{C}}_{\ell_i}(\nu_1,\nu_2)$ from simulated signal.

Next, we compute the system noise MAPS at cells $\boldsymbol{U}_{\rm g}=\boldsymbol{\ell}_{\rm g}/(2\pi)$ using (e.g. White et al. 1999; Zaldarriaga, Furlanetto & Hernquist 2004; Mondal et al. 2020a)

$$\mathcal{C}^{\rm N}_{\ell_{\rm g}}(\nu,\nu)=\frac{8\,{\rm h}}{t_{\rm obs}\,\tau_8(\boldsymbol{U}_{\rm g})}\times\frac{T^2_{\rm sys}\,\lambda^4}{N_{\rm p}\,\Delta t\,\Delta\nu\,a^2\int{\rm d}\boldsymbol{U}'|\tilde{A}(\boldsymbol{U}-\boldsymbol{U}')|^2}\,, \tag{7}$$

where ν is the observing frequency and $\Delta\nu$ is the corresponding channel width. In the equation above, $t_{\rm obs}$ is the total observation time and $\tau_8(\boldsymbol{U}_{\rm g})$ denotes the gridded baseline distribution considering uv tracks of 8 h per night observations. One need to adjust the 8 h in the numerator in case the baseline tracks have been simulated for different observation hours per night. Here, we consider the system temperature $T_{\rm sys}$ to be a sum of sky temperature $T_{\rm sky}=60\lambda^{2.55}$ K (e.g. Reich & Reich 1988; Platania et al. 1998; Rogers & Bowman 2008; Bernardi et al. 2009; Fixsen et al. 2011; McKinley et al. 2018; Mozdzen et al. 2018; Spinelli et al. 2021) and the receiver temperature $T_{\rm rec}$ (e.g. Shaw et al. 2019; Mondal et al. 2020a). Note that the λ considered in $T_{\rm sky}$ is in metres and $T_{\rm rec}$ is the amplitude of the white Gaussian noise generated by the antenna receiver. $N_{\rm p}=2$ is number of dipole polarization, $\Delta t=60$ s is the integration time for each baseline, $\Delta\nu$ is the frequency channel width, a^2 is the physical area of each antenna element, and $\tilde{A}(\boldsymbol{U})$ is the Fourier transform of the antenna beam pattern $A(\boldsymbol{\theta})$. For simplicity, we consider each antenna element to be circular with a diameter D. Considering circular symmetry, we approximate the main lobe of the primary beam by a Gaussian $A(\theta)=\exp(-\theta^2/\theta_0^2)$ (Choudhuri et al. 2014; Mondal et al. 2020a). The computation of system noise MAPS (equation 7) at every $\boldsymbol{U}_{\rm g}$ cell depends on various design specifications of the telescopes which are tabulated in Table 2.

We now consider a non-uniform weighting scheme as the system noise contribution varies across the cells $\boldsymbol{U}_{\rm g}$ for the noisy observational data. We obtain the weights at every cells by maximizing the signal-to-noise ratio which is defined as $SNR^{\ell_i}_{12}\equiv\bar{\mathcal{C}}_{\ell_i}(\nu_1,\nu_2)/\boldsymbol{\sigma}^{\ell_i}_{12}$. We make a simplifying assumption that the 21-cm MAPS does not vary significantly across the cells within a particular bin, i.e. $\mathcal{C}_{\ell_{\rm g_i}}(\nu_1,\nu_2)=\bar{\mathcal{C}}_{\ell_i}(\nu_1,\nu_2)$. Under this assumption, we find that the non-normalized weights can be written as (see e.g. Feldman, Kaiser & Peacock 1994; Mondal et al. 2020a)

$$\begin{aligned}\hat{w}_{\rm g_i} &= [\{\bar{\mathcal{C}}_{\ell_i}(\nu_1,\nu_1)+\mathcal{C}^{\rm N}_{\ell_{\rm g_i}}(\nu_1,\nu_1)\}\{\bar{\mathcal{C}}_{\ell_i}(\nu_2,\nu_2)+\mathcal{C}^{\rm N}_{\ell_{\rm g_i}}(\nu_2,\nu_2)\} \\ &\quad+\{\bar{\mathcal{C}}_{\ell_i}(\nu_1,\nu_2)+\delta^{\rm K}_{\nu_1,\nu_2}\mathcal{C}^{\rm N}_{\ell_{\rm g_i}}(\nu_1,\nu_1)\}^2]^{-1}, \end{aligned} \tag{8}$$

where $w_{\rm g_i}=\hat{w}_{\rm g_i}/\sum_{\boldsymbol{U}_{\rm g_i}}\hat{w}_{\rm g_i}$. The weight (equation 8) here varies inversely to square of system noise power spectrum $\mathcal{C}^{\rm N}_{\ell}(\nu,\nu)$, hence cells with larger noise contaminations will contribute less to the bin-averaged MAPS and *vice-versa*. The cells which do not have uv sampling (i.e. $\tau_8(\boldsymbol{U}_{\rm g})=0$) equivalently have infinite noise (equation 7). Using the weight in equation (6) the variance in $\bar{\mathcal{C}}_{\ell_i}(\nu_1,\nu_2)$ can be written as

$$[\boldsymbol{\sigma}^{\ell_i}_{12}]^2=\frac{1}{2}\times\frac{1}{\sum_{\boldsymbol{U}_{\rm g_i}}\hat{w}_{\rm g_i}}. \tag{9}$$

Next, considering the diagonal elements where MAPS $\bar{\mathcal{C}}_{\ell_i}(\nu,\nu)$ peaks, the corresponding variance (equation 6) can further be reduced down to

$$[\boldsymbol{\sigma}_{11}^{\ell_i}]^2 = \frac{1}{\sum_{\boldsymbol{U}_{g_i}}[\bar{\mathcal{C}}_{\ell_i}(\nu_1,\nu_1)+\mathcal{C}^{\rm N}_{\ell_{g_i}}(\nu_1,\nu_1)]^{-2}}. \tag{10}$$

We finally use equation (10) to compute the error variance in the measurements of $\mathcal{D}_\ell(\nu,\nu)$ for our fiducial model (M3-$f_{\rm X}$10). We present the results for three current and upcoming radio-interferometers *HERA*, *NenuFAR*, and *SKA-Low* below.

4.2 Detectability with *HERA*

The *HERA* is a radio-interferometric telescope located in the Karoo desert, South Africa. It consists of zenith pointing dishes of 14 m diameter which are arranged in a closed packed hexagonal core of about 300 m across. Currently this telescope is observing in its first phase with 50 dishes and within frequency bandwidth 100–200 MHz that spans EoR. In this analysis, we consider the whole frequency bandwidth is divided into 1024 channels having channel width 97.66 kHz. Recently, Abdurashidova et al. (2022) and The HERA Collaboration et al. (2022) have put best upper limits to date on EoR 21-cm 3D power spectrum by analysing roughly 1000 h of *HERA* Phase I data. In its final phase, the array will consists of total 350 dishes all observing within a larger frequency range 50–250 MHz which covers both the CD and EoR (see e.g. Fagnoni et al. 2021). We consider the upcoming final phase of *HERA* for our predictions here. We simulate baseline tracks of *HERA* observing in drift scan mode at a declination DEC=$-30^\circ43'17''$ (phase centre of the telescope). We finally compute the total error variance $[\boldsymbol{\sigma}_{12}^{\ell_i}]^2$ using equation (9) where we set $T_{\rm rec}=170$ K (see Table 2) which is similar to that of the Phase I receivers (see e.g. Thyagarajan et al. 2020; Fagnoni et al. 2021). Note that the common square ℓ plane which is used for *HERA* predictions extends between ± 11250 with cell size being $\Delta\ell = 97.82$. We divide this accessible ℓ plane into 10 log-spaced circular bins for estimating the errors.

Unlike field tracking, the sky patch which *HERA* is looking at constantly changes with time in drift-scan mode. Thus, we can say that at every integration time-stamp *HERA* measures a different realization of the signal. This gives rise to additional CV in the 21-cm MAPS measured at every voxel. Based on this intuition, we add the contribution of this excess variance in quadrature to equation (10) for simplicity. Assuming the fluctuations in the MAPS due to drifting sky patch to be Gaussian, we expect the additional variance in the diagonal MAPS to be proportional to the average measurement, i.e. $\mathcal{D}^2_\ell(\nu,\nu)/N_{\rm snap}$. The number of snapshots of the different sky patch drifting per night of observations $N_{\rm snap}$ is set by the integration time of the interferometer. Here we consider *HERA* observing 8 h per night with 60 s integration time resulting into $N_{\rm snap}=480$. One can decrease the integration time for a fixed observing hours per night to reduce this excess CV. However, one can always compute the total error variance starting from the scratch but it is not straightforward. We defer this to our future analysis with *HERA*. We would like to emphasize that this change is incorporated only for *HERA*, and not for the *NenuFAR* or *SKA-Low*.

Fig. 10 shows the predictions for observing the diagonal of 21-cm MAPS $\mathcal{D}(\nu,\nu)$ for four different ℓ bins in four panels. Every panel here is divided into two subpanels where, in the top subpanel we show the $\mathcal{D}(\nu,\nu)$ (thick blue lines) along with 2σ error estimates (i.e. $2\boldsymbol{\sigma}_{11}^{\ell_i}$) for different observation time $t_{\rm obs}$, and in the bottom subpanel we plot sound-to-noise ratio (SNR) for the corresponding $t_{\rm obs}$ values. Here, we have assumed that the foreground is perfectly modelled and completely removed from the observed data. However, this is not the case for *HERA* which avoids 'foreground wedge' in the $(\boldsymbol{k}_\perp, k_\parallel)$ plane (e.g. Datta et al. 2010; Pober et al. 2013) to mitigate foregrounds in power spectrum estimation. Therefore, the results presented below are optimistic and provide upper limits to the sensitivity. One can follow the method described in section 6 of Mondal et al. (2020a) to incorporate the effect of foreground avoidance in an approximate way. However, we restrict ourselves to foreground removal in order to make a fair comparison with *NenuFAR*. Note that we fix 2σ as the detection criterion in this paper. Considering any panel, the solid red and the solid orange lines represent the 2σ total error (top subpanel) and the corresponding SNR (bottom subpanel), respectively, for $t_{\rm obs}=104$ and 1000 h. We also plot the system noise contribution to the total error by red and orange dotted lines, respectively, for both $t_{\rm obs}=104$ and 1000 h in the top subpanels. We also plot the 2σ CV (green dashed line) which is inherent to the signal and can be achieved after hypothetically integrating the system noise for $t_{\rm obs}\rightarrow\infty$. The dot–dashed grey line in each of the bottom subpanels demarcates the floor SNR $=2$ above which we claim it to be a detection.

Considering $\ell=343$ (top-left panel), we find that the 21-cm MAPS will be detectable (i.e. SNR ≥ 2) for $t_{\rm obs}=104$ h within frequency range 80–132 MHz which contains the heating peak for our fiducial model. The SNR here can go as high as 4 at $\nu\sim 110$ MHz which is closer to the CV limit. Increasing $t_{\rm obs}$ is expected to improves the SNR $\propto t_{\rm obs}$ for frequencies where the total error is dominated by system noise ($\nu > 130$ MHz). For $t_{\rm obs}=1000$ h, we find that 21-cm MAPS at $\ell=343$ can be measured roughly across the full CD–EoR ($\nu > 75$ MHz). We also note that the system noise contribution $\sigma_{\rm N}$ increases rapidly towards the smaller frequency as the sky becomes brighter at large redshifts (see equation 7). Considering the next bin at $\ell=538$ (top-right panel), we find that the signal MAPS as well as its CV do not change much. However, we find that $\sigma_{\rm N}$ relatively increases thereby increasing the total error in the measurement. This restricts the detection of the 21-cm MAPS to a narrower frequency range, i.e. between $\nu=96$–130 MHz for 104 h and $\nu\gtrsim 82$ MHz for 1000 h. We find that $\sigma_{\rm N}$ contribution to total error increases rapidly towards the larger ℓ values (small-scales). This is due to the decrease of baseline distribution $\tau_8(\boldsymbol{U}_{g_i})$ towards larger $U=\ell/(2\pi)$, and this decreases in baseline density is very rapid for compact arrays such as *HERA*. From the bottom panels of Fig. 10, we note that 104 h of observations will be able to measure the 21-cm MAPS only within $\nu\approx 100$–120 MHz for $\ell=853$ where the CD MAPS peaks. For $t_{\rm obs}=1000$ h the 2σ detection is restricted only to limited frequency ranges between 87–132 MHz for $\ell=853$ and 100–125 MHz for $\ell=1347$. The SNR drops considerably for any bins larger than $\ell=1347$ due to sudden fall in baseline sampling on the cells $\boldsymbol{U}_{\rm g}$.

4.3 Detectability with *NenuFAR*

NenuFAR[3] is an extension of the current *LOFAR*[1] telescope that has been installed very recently at the Nançay Radio Observatory in France. It is expected to consist of 96 core stations (also known as mini-arrays) which are distributed within a compact circle of ~ 400 m in diameter (Mertens, Semelin & Koopmans 2021). Apart from the compact core, it will have six more mini-arrays as remote-stations. Currently, *NenuFAR* has 80 core and two remote stations rolled out and rest will be installed in future. Each mini-array consists of 19 crossed dipole antennas arranged within a regular hexagonal pattern. *NenuFAR* operates within a frequency bandwidth of 10–85 MHz that corresponds to a redshift range $z\approx 16$–140 spanning CD and dark ages. *NenuFAR* has already started its first phase of

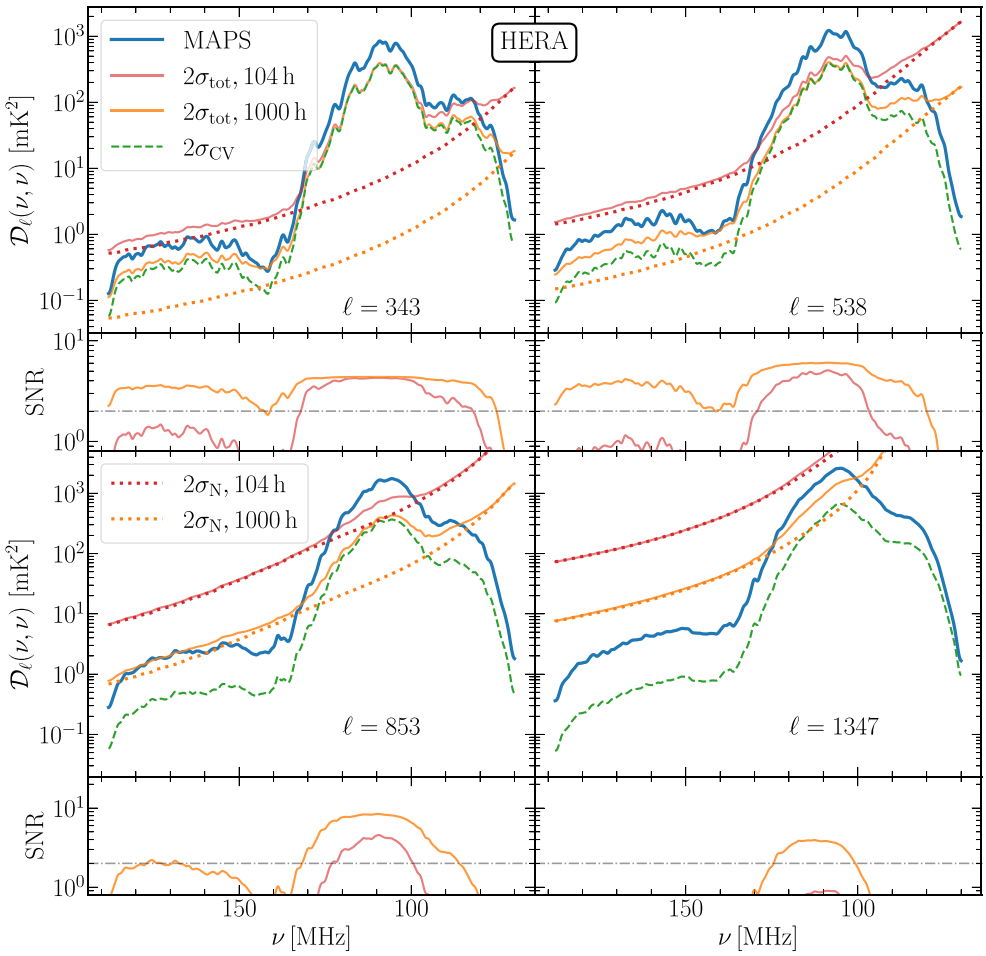

Figure 10. *HERA* predictions for detecting the diagonal ($\nu_1 = \nu_2$) of the scaled MAPS $\mathcal{D}_\ell(\nu,\nu) = \ell(\ell+1)\mathcal{C}_\ell(\nu,\nu)/(2\pi)$. The four panels here correspond to the different ℓ bins as labelled. The thick solid blue lines show the expected CD–EoR 21-cm MAPS as a function of ν corresponding to M3-$f_{\rm X}$10. The red and orange solid lines in the four bigger panels represent the total 2σ error estimates considering 97.66 KHz channel-width, respectively, for 104 and 1000 h of *HERA* drift-scan observations. Corresponding dotted red and orange lines represent the system noise contribution (2σ) to the total error for 104 and 1000 h, respectively. The dashed green lines in the four bigger panels represent the respective CV error estimates (2σ). The four smaller panels, corresponding to the bottom of each bigger panel, show how SNR of the measurements varies with the observing frequency ν for 104 h (red) and 1000 h (orange). The grey dashed lines in the smaller panels demarcate SNR = 2 floor for detection.

observations. We consider the channel width for *NenuFAR* to be twice of *HERA*, i.e. 195.2 kHz. In this work, we consider a mock observation tracking a field at DEC=+47°22′34″ with the final phase of *NenuFAR* having 102 mini-arrays. As *NenuFAR* operates in a very low frequency band, its $T_{\rm rec}$ is expected to be larger compared to the other telescopes considered here. For the purpose of this work, we have assumed a mean value of $T_{\rm rec} = 1000$ K[12] (see Table 2) which remains smaller than $T_{\rm sky}$ at the relevant frequencies.

Note that our LC boxes span a frequency range between ≈70 and 200 MHz where the X-ray heating, which is important during CD, becomes effective at $\nu > 80$ MHz for our fiducial model M3-$f_{\rm X}$10 (see Figs 1 and 2). This does not overlap at the low-frequency end with the observational frequency bandwidth of *NenuFAR*. Hence, we artificially shift our LC box by 40 MHz towards smaller frequencies. The shifting in frequency, in principle, demands a change in $\delta_{\rm B}$ and therefore $\delta T_{\rm b}(\boldsymbol{x}, \nu)$ due to evolution in background cosmology. However, for this analysis, we have assumed that the effect of the change in cosmology can possibly be overridden by properly tuning the physical processes by tweaking the relevant CD parameters within its uncertainties. We finally use the shifted LC box to make predictions for *NenuFAR*. The prediction here is to demonstrate the detectability of the *NenuFAR* in case the CD falls within its frequency bandwidth, and cannot be directly compared with that of *HERA*. A better treatment of the signal is required for more accurate predictions and that we defer to our future work which will be devoted to *NenuFAR*.

As we have shifted the box in frequency, the extent of the accessible ℓ plane for *NenuFAR* will be a little different from *HERA*. Here, the square ℓ plane has extent between ±12 093 with $\Delta\ell = 108.95$, and we divide this also in 10 log-spaced circular bins. Fig. 11 shows the predictions for measuring 21-cm MAPS using *NenuFAR*. Note that the following prediction considers an optimistic scenario where the foreground is assumed to be completely removed from the observed data. The plot is arranged in a similar way as in Fig. 10, except here we plot the 2σ errors and SNR for 1000, 5000, and 10 000 h in orange, red, and cyan lines, respectively. Our choices of $t_{\rm obs}$ here is not completely unrealistic as the data for more than 1000 h of

[12] nenupy.readthedocs.io/en/latest/instru/instrument_properties.html

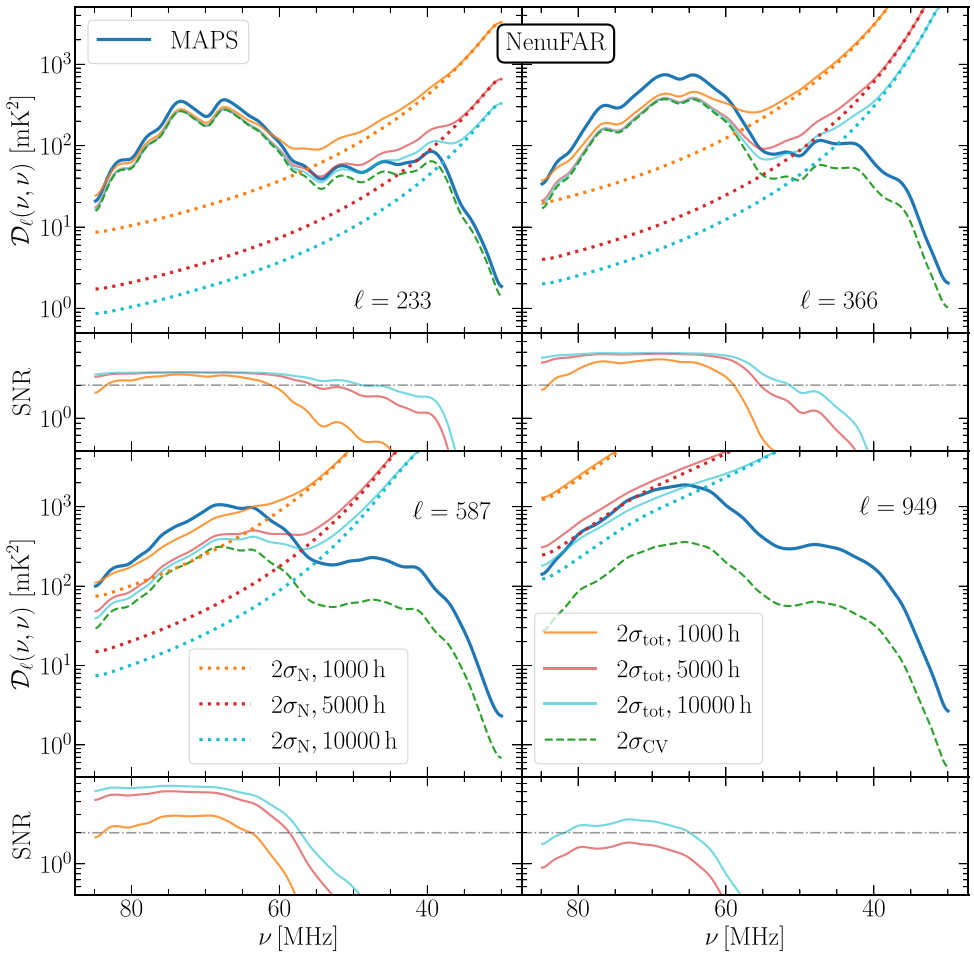

Figure 11. *NenuFAR* predictions for detecting the diagonal ($\nu_1 = \nu_2$) of the scaled MAPS $\mathcal{D}_\ell(\nu,\nu) = \ell(\ell+1)\mathcal{C}_\ell(\nu,\nu)/(2\pi)$. The four panels correspond to the different ℓ bins as labelled. The thick solid blue lines show the expected CD–EoR 21-cm MAPS as a function of ν corresponding to M3-$f_{\rm X}$10. The red, orange, and cyan solid lines in the four bigger panels represent the total 2σ error estimates, respectively, for 1000, 5000, and 10 000 h of *NenuFAR* observations. Corresponding dotted red, orange, and cyan lines represents the system noise contribution (2σ) to the total error for 1000, 5000, and 10 000 h, respectively. The dashed green lines in the four bigger panels represent the respective CV error (2σ) estimates. The four smaller panels, corresponding to the bottom of each bigger panel, show how SNR of the measurements varies with the observing frequency ν for 1000 h (red), 5000 h (orange), and 10 000 h (cyan). The grey dashed lines in the smaller panels demarcate SNR = 2 floor for detection.

observations have already been acquired with *NenuFAR*. Considering the smallest bin at $\ell = 233$ (top-left panel of Fig. 11), we find that 1000 h of *NenuFAR* observations can measure the X-ray heating peak of 21-cm MAPS only within 20 MHz band around $\nu = 70$ MHz with SNR $\gtrsim 2$. Increasing $t_{\rm obs}$ to 5000 or 10 000 h pushes the system noise contribution $\sigma_{\rm N}$ well below the CV error $\sigma_{\rm CV}$ at $\nu \gtrsim 50$ MHz and the total error $\sigma_{\rm tot}$ approaches the CV limit. We find that a detection between 55 and 85 MHz is possible with $2 <$ SNR < 3. The SNR achieved for this bin is low due to small number of $\boldsymbol{U}_{\rm g}$ cells resulting into a larger CV contribution.

Moving to next bin, i.e. $\ell = 366$ (top-right panel), the relative contribution of CV to the total error decreases as expected. The system noise and the 21-cm MAPS is seen to increase in a similar proportion thereby improving the SNR as compared to $\ell = 233$. We find that, for this bin and $t_{\rm obs} = 1000$ h, the 21-cm MAPS will be detected within a frequency range 58–84 MHz with $2 \leq$ SNR ≤ 3. This frequency range further expands to ν between 55–85 MHz and 50–85 MHz for $t_{\rm obs} \geq 5000$ and 10 000 h, respectively, with SNR becoming as large as 4. The detection is still not possible for $\nu \lesssim 55$ MHz as the system noise increases rapidly with decreasing ν for larger ℓ values due to a decrease in the baseline density distribution.

The system noise contribution increases further for $\ell = 587$ (bottom-left panel), where we note that $t_{\rm obs} = 1000$ h is able to measure the peak of the MAPS within 64–84 MHz at $2 \leq$ SNR ≤ 3. For $t_{\rm obs} = 5000$, the frequency range of the detected MAPS increases to 58–85 MHz with a maximum SNR ≈ 5. This further improves for $t_{\rm obs} = 10\,000$ h, however, not significantly. As is apparent from Fig. 11, the CV contribution $\sigma_{\rm CV}$ decreases towards larger ℓ values (bottom panels) as there are more cells. However, the contribution from $\sigma_{\rm N}$ increases at a faster rate with increasing ℓ. This is due to the fact that the baseline density distribution decreases rapidly at large *uv* distances because *NenuFAR* has fewer correlated receiver elements (mini-arrays) than *HERA*. Considering $\ell = 949$ (bottom-right panel), which is almost dominated by system noise, we note that $t_{\rm obs} \gtrsim 10\,000$ h of observations is required to measure the signal MAPS at SNR ≥ 2 and that still within a narrow frequency band around $\nu = 70$ MHz. The system noise increases very rapidly for the bins with $\ell \gtrsim 1000$ for *NenuFAR* making it impractical to measure the signal MAPS at small-angular scales.

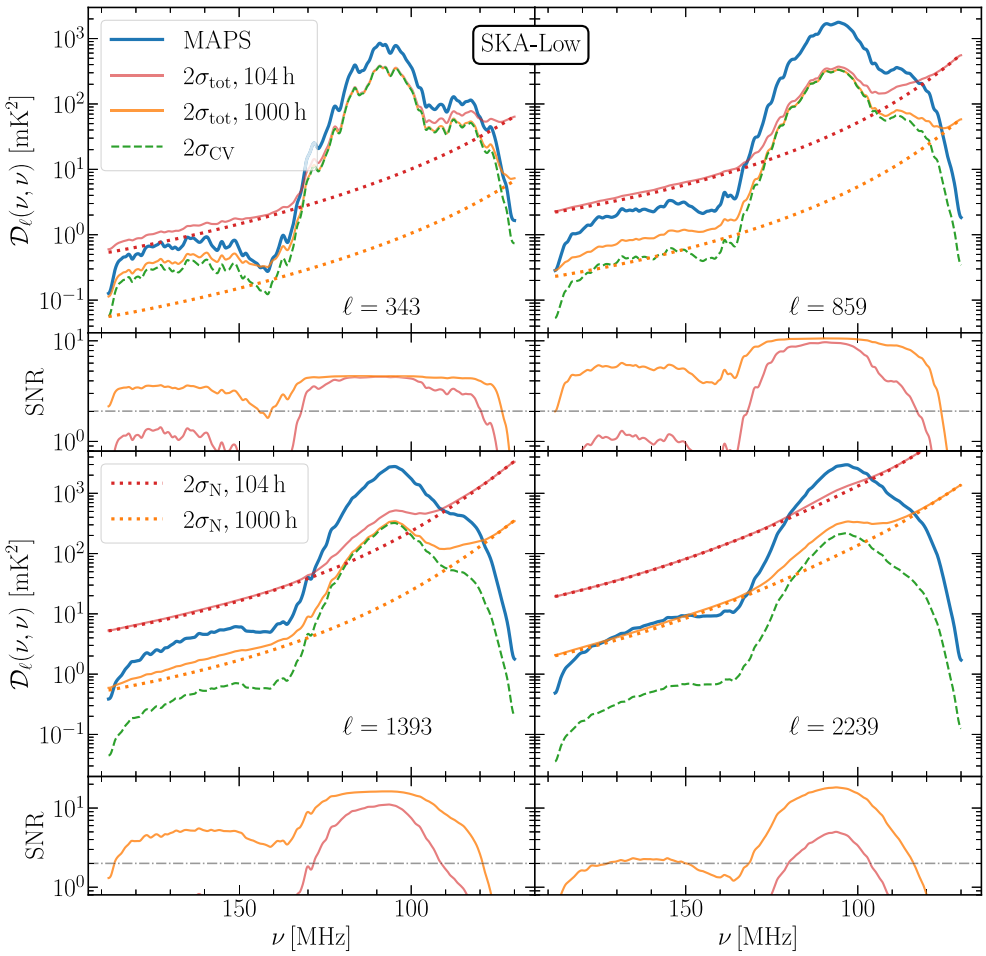

Figure 12. *SKA-Low* predictions for detecting the diagonal ($\nu_1 = \nu_2$) of the scaled MAPS $\mathcal{D}_\ell(\nu,\nu) = \ell(\ell+1)\mathcal{C}_\ell(\nu,\nu)/(2\pi)$. The arrangement of this plot is the same as in Fig. 10.

4.4 Detectability with *SKA-Low*

The *Square Kilometer Array* (*SKA*[7]) is going to be world's largest radio telescope which is expected to be completed by the end of this decade. It consists of two arrays—(i) *SKA-Mid*, which is being built at the Karoo desert in South Africa and will operate within the frequency range of 350–15300 MHz and (ii) *SKA-Low*, which is being built at Murchison Radioastronomy Observatory in Western Australia and will operate within the frequency range of 50–350 MHz. *SKA-Low* will be suitable for the CD–EoR measurements (Koopmans et al. 2014) as it can observe 21-cm signal coming from the redshifts between $z = 3$ and 27. Here, we consider the channel width of *SKA-Low* to be the same as *HERA*, i.e. 97.66 kHz. *SKA-Low* will have ∼131 thousands log-periodic dipoles which will be distributed among 512 stations in its final phase. Each of the stations will have 256 dipoles that will be scattered within a diameter of 35 m. The antenna layout of *SKA-Low* will have a compact core with roughly 50 per cent of stations lying within a diameter of ∼1 km. The remaining stations will be grouped into clusters of six stations and these clusters will be arranged in three modified spiral arms such that the maximum baseline length will be ∼64 km (Dewdney & Braun 2016). Here, we consider an observation with *SKA-Low* tracking a field at DEC=−26°49′29″ for 8 h per night. We use the resulting baseline tracks to predict the errors in measuring MAPS with this telescope. For *SKA-Low*, we have used similar ℓ plane and binned it on the same way as for *HERA*.

Fig. 12 shows the errors estimated in the measurements of $\mathcal{D}_\ell(\nu,\nu)$ for $t_{\rm obs} = 104$ and 1000 h, just as we have presented for *HERA* but for $\ell = 343$, 859, 1393, and 2239. We note that, the predictions here also consider foreground removal for comparison on similar grounds. The colour scheme of this figure is exactly the same as that in Fig. 10. Comparing *SKA-Low* with the previous telescopes, it is able to perform far better in terms of sensitivity (Figs 10, 11, and 12). Also having a denser baseline distribution and longer *uv* extent allows *SKA-Low* to measure MAPS on smaller scales ($\ell \approx 5000$) compared to compact arrays such as *HERA* and *NenuFAR*. Considering the four panels of Fig. 12, we note that *SKA-Low* will be able to measure the CD 21-cm MAPS with 104 h of observations. We find that a 2σ measurement is possible within the frequency ranges 80–132 MHz, 82–132 MHz, 90–128 MHz, and 96–120 MHz, respectively, for $\ell =$ 343, 859, 1393, and 2239. We find that the system noise contribution to the total error $\sigma_{\rm tot}$ drops considerably for $t_{\rm obs} = 1000$ h allowing SNR to rise above the detection limit of 2 in almost the whole frequency bandwidth for the four ℓ bins considered here. However, the SNR does not improve much around the X-ray heating peak in 21-cm MAPS ($\nu \approx 100$ MHz) by increasing $t_{\rm obs}$ beyond 104 h for $\ell \lesssim 1000$ as the $\sigma_{\rm tot}$ is dominated by $\sigma_{\rm CV}$. In such cases, it is better

to divide the total observation hours over multiple independent sky-patches. This can be done for the field-tracking instruments such as *NenuFAR* and *SKA-Low*. Combining the data incoherently from different fields will help in beating down the CV to the measured MAPS (e.g. Koopmans et al. 2014).

Considering top panels for $t_{\rm obs} = 1000$ h, we find that the measurement of 21-cm MAPS is possible for $\nu \geq 75$ MHz with maximum SNR ≈ 4 and 10, respectively for $\ell = 343$ and 859. However, we note that the detection is possible at $\nu \geq 80$ MHz for $\ell = 1393$ and between 85 and 170 MHz for $\ell = 2239$. The maximum value of SNR saturates to values near 15 where $\sigma_{\rm tot}$ is dominated by CV for $\ell = 1393$. For $\ell = 2239$ the SNR rises further to a maximum value of 20 near the heating peak ($\nu \approx 105$ MHz) of the 21-cm MAPS. The system noise contributions $\sigma_{\rm N}$ to $\sigma_{\rm tot}$ gradually increases in the larger ℓ bins as the baseline density decreases. This further starts decreasing the SNR, and it requires larger values of $t_{\rm obs}$ to achieve a sufficient SNR to detect the signal from small angular-scales (large ℓ).

5 SUMMARY AND DISCUSSIONS

The measurements of brightness temperature fluctuations $\delta T_{\rm b}$ of the redshifted 21-cm radiation from the H I provide a unique way to unveil the secrets of formation of the first luminous objects in the Universe. The primary goal of all existing and future radio-interferometric experiments (e.g. *LOFAR*, *MWA*, *HERA*, *NenuFAR*, *uGMRT*, and *SKA-Low*) is to measure the 3D power spectrum $\Delta^2_{\rm b}(k, z)$ of the fluctuating 21-cm signal coming from the CD and EoR. The definition of 3D power spectrum inherently assumes the signal to be statistically homogeneous and isotropic along all directions of the signal volume. However the CD–EoR 21-cm signal in real observations is not statistically homogeneous and isotropic along the LoS direction of the observed volume due to LC effect (Barkana & Loeb 2006). The LC effect on the $\Delta^2_{\rm b}(k, z)$ is considerable for EoR 21-cm signal at least on large-scales (e.g. Datta et al. 2012; Zawada et al. 2014; Mondal et al. 2018). This effect on 3D power spectrum becomes considerable during CD when the 21-cm signal is controlled by the spin-temperature fluctuations driven by the X-ray sources (Ghara et al. 2015b). Also, we find that the deviations in 3D power spectrum due to LC effects during CD can be as large as ± 100 per cent for our fiducial model (M3-$f_{\rm X}10$) at scales corresponding to $k = 0.15$ Mpc^{-1} (see Fig. 3). The deviations are found to decrease on small scales ($k = 1.1$ Mpc^{-1}), however they are still closer to ± 100 per cent for our fiducial model. Note that, here we consider a large comoving volume $V = [500h^{-1}$ Mpc$]^3$ which corresponds to a frequency bandwidth $\sim$40 MHz at relevant frequencies which are not very unrealistic for the *HERA* and *SKA-Low*. However the LC effects will be less pronounced if the data is analysed within a smaller frequency band, say $\sim$10 MHz, as is being done for *LOFAR*, *NenuFAR*, etc.

The MAPS (equation 3) provides an unbiased alternative to the 3D power spectrum. In this work, we use the bin-averaged MAPS (Mondal et al. 2018) estimator (equation 4) to quantify the two-point statistics of the simulated (see Section 2.1) LC of the CD–EoR 21-cm signal. We find that the diagonal 21-cm MAPS $\mathcal{D}_\ell(\nu, \nu)$ captures the signatures of cosmic evolution of the signal more distinctly than the 3DPS (see Figs 3, 7, and 9) when analysed within a large-bandwidth signal volume. However, this is a matter of binning and analysing the data. It is still possible to see the distinct evolutionary features in 3DPS by computing it from the data divided into small-bandwidth chunks, within which the signal is considerably correlated (see Fig. 5). Analysing data in small bandwidths reduces the LC bias in the 3DPS estimates, if not removed. The shape and the amplitude of the 21-cm MAPS are sensitive to the properties of the sources and the processes driving CD–EoR. This extra information has been tentatively shown to provide more stringent constraints over the EoR model parameters than the 3DPS (Mondal et al. 2022). In a future work, we plan to explore the impact of MAPS on the CD model parameter estimation, relative to the 3DPS.

Considering a model where the spin temperature is saturated and $T_{\rm s} >> T_\gamma$ (here M1), we only see a dip around a point where the reionization starts and a peak when IGM is ~ 50 per cent ionized. This feature in the MAPS of model M1 is distinctly different from the other models (see Table 1) where X-ray heating is included in the simulations self-consistently from the beginning. We also note that the 21-cm MAPS of M1 is roughly two orders of magnitude smaller than that of the other models with self-consistent evolution of $T_{\rm s}$. In the other two models M2 and M3, the unsaturated X-ray heating boosts 21-cm MAPS during CD by introducing additional fluctuations in $\delta T_{\rm b}$ through $T_{\rm s}$. We distinctively note a peak like feature around $\nu = 110$ MHz in the diagonal and near-diagonal elements (see Figs 4 and 7) for models M2-$f_{\rm X}10$ and M3-$f_{\rm X}10$. The location of the heating peak and its width depends upon the X-ray efficiency $f_{\rm X}$ of the sources in the IGM as seen in Figs 8 and 9. We also note another peak in 21-cm MAPS around $\nu = 90$ MHz which arises due to fluctuations in the Ly-α coupling in the model M3-$f_{\rm X}10$ (see Figs 8 and 9). The peak is prominent for large angular-scales (small ℓ) and it gradually merges with the heating peak and disappears as we move to the large ℓ values.

We also find the correlations between the signal at different frequencies (ν_1, ν_2) significantly drops roughly beyond $\Delta\nu = \pm 3$ MHz (Fig. 5). The rate of decorrelation depends upon the concerned epoch and also it can be related to the mean free path of the photons which plays important role in governing the signal during that epoch. We note that the epoch where X-ray heating plays important role ($\nu \approx$ 100–140 MHz), the signal remains positively correlated over a larger frequency range (see Figs 4, 6, and 8) as the X-rays can travel farther. On the other hand, the decorrelation during EoR is faster as the mean free path of the UV photons is much less than that of the X-rays.

The observed 21-cm signal from CD–EoR gets contaminated with the system noise, foregrounds, radio frequency interference, and other systematics. This contributes to the error in the measurement of 21-cm MAPS along with the inherent CV. In this work, we present the detectability of the 21-cm MAPS $\mathcal{D}(\nu, \nu)$ in the context of future observation using *HERA*, *NenuFAR*, and *SKA-Low*. We estimate the expected errors in the measured 21-cm MAPS considering the observed signal to be free from systematics, foregrounds, and RFI. We note that *NenuFAR* follows the foreground removal strategy, whereas *HERA* is designed to avoid the foreground wedge in their power spectrum analysis. However, for an equal comparison, we assume that foreground is perfectly subtracted from the data, for every telescope considered here, which leads to optimistic sensitivity predictions. Here, we assume that the 21-cm signal is statistically equivalent to a Gaussian random field and ignore the impact of trispectrum in the CV measurements (e.g. Mondal et al. 2016). The contribution from non-Gaussianity to the error estimates can be important only during later stages of EoR where the trispectrum becomes comparable or stronger than the Gaussian system noise contribution (Shaw et al. 2019). During CD, the Gaussian system noise will be much larger than the inherent non-Gaussianity of the signal.

We find that 104 h of *HERA* drift scan observations will be able to provide the CD 21-cm MAPS (diagonal elements) at $>2\sigma$ level

for $\ell \lesssim 1000$ with the errors being dominated by CV below $\ell \approx 400$ (see Fig. 10). With 1000 h of observations, we can achieve $>2\sigma$ measurement of CD 21-cm MAPS for $\ell \lesssim 1800$. *HERA* is able to measure the EoR 21-cm MAPS only for $\ell < 850$ with 1000 h observations. We can obtain the maximum SNR of ≈8 with 1000 h of data for the bin corresponding to $\ell = 853$ (see Fig. 10). Increasing the observation hours further can increase the SNR up to 10 which is fixed by the CV for this bin. The sensitivity of *HERA* decreases for larger ℓ bins due to compact baseline distribution and we cannot measure signal beyond $\ell = 1800$.

The upcoming *SKA-Low* is expected to outperform *HERA* in terms of sensitivity due to denser baseline densities. The system noise contribution is much less for *SKA-Low* that the total error in the measurement of CD 21-cm MAPS is dominated mostly by the CV contribution for $\ell \lesssim 1000$ with $t_{\rm obs} = 104$ h. Increasing $t_{\rm obs}$ further to 1000 h does not improve the SNR much for the CD signal. However the detectability improves considerably for the EoR 21-cm MAPS and it reaches SNR > 2 for $t_{\rm obs} = 1000$ h. The system noise increases and becomes comparable with the CV contribution for $\ell > 1000$, however it is still possible to measure the peak of the CD 21-cm MAPS with $t_{\rm obs} = 104$ h for $\ell < 5000$. The EoR 21-cm MAPS can only be detected at SNR > 2 within $\ell < 2240$, but for $t_{\rm obs} = 1000$ h. The SNR for *SKA-Low* can be as high as 10 and 20, respectively, for $t_{\rm obs} = 104$ h and 1000 h even at intermediate scales of $\ell \sim 1000$ (see Fig. 12).

NenuFAR operates in a frequency band 10–85 MHz which probes the 21-cm signal farther in redshift than *HERA* and *SKA-Low*. It has channels which are twice as wide as for *HERA* and *SKA-Low*. Given this mismatch in the frequency band with the other telescopes, we consider a different CD–EoR model for *NenuFAR* predictions. This new model assumes that heating started at earlier redshifts such that the strong impact of spin temperature fluctuations falls within the frequency band of *NenuFAR*. If the peak of CD 21-cm MAPS falls in the range of *NenuFAR*, it will be possible to measure it at SNR > 2 for $\ell \lesssim 600$ with $t_{\rm obs} = 1000$ h (see Fig. 11). The SNR will improve if $t_{\rm obs}$ is increased to say 5000 h or 10 000 h but the noticeable change is only restricted to a narrow range of $360 < \ell < 600$. The reason for such large error in the measurement is the system noise contribution which increases very rapidly towards large redshifts. It is not possible to achieve an SNR ≥ 2 per frequency channel even with $t_{\rm obs} = 10\,000$ h beyond $\ell = 1000$.

The whole point of computing MAPS by correlating the 21-cm signal across the frequency channel elements is for keeping the LC evolution information from the signal volume. However, analysing the data over small frequency channels makes the 21-cm MAPS statistics suffer from the noise contribution. Whereas in 3DPS, we analyse the data over a large frequency bandwidth that effectively reduces the noise contribution in 3DPS estimates. Contradicting the philosophy behind MAPS, one can anyway improve the SNR of the MAPS measurements by combining the observed signal in consecutive frequency channels. This way of beating down noise is effective only when the measurement error is dominated by the system noise such as in the case of *NenuFAR*. We find that averaging the signal within a frequency band of 5 MHz around the CD MAPS peak frequency considerably improves the integrated SNR for *NenuFAR* (see the last column of Table 3). However, there is small change for *HERA* and negligible change for *SKA-Low* as compared to the SNR per channel estimated at $\ell \sim 550$ for $t_{\rm obs} = 1000$ h. This is because the error is CV dominated for both *HERA* and *SKA-Low*.

It is possible to further reduce the CV and improve SNR for field-tracking instruments (e.g. *SKA-Low* and *NenuFAR*) by breaking up one long observation (say ≥1000 h) to shorter observations targeting different sky-patches and combining them afterwards. However, the division should be such that the system noise SNR computed from an individual patch remains well above unity (e.g. Koopmans et al. 2014). Nonetheless the channel averaging can still be useful to achieve a decent integrated SNR for *HERA* and *SKA-Low* at large ℓ and/or for smaller $t_{\rm obs}$ where the system noise remains dominant. However, one needs to choose the frequency range carefully such that the 21-cm signal MAPS does not decrease too much especially near the peaks.

Our study finally concludes that it will be possible to measure the CD–EoR 21-cm MAPS within reasonable observation time using the current and upcoming radio-interferometers mentioned in this paper. Incorporating the effects of foregrounds, however, can degrade the prospect of detection (Mondal et al. 2020a). We also ignore the effects of non-Gaussianity of the 21-cm signal which can affect the error predictions and hence the detectability, especially during the mid and later stages of EoR. It is therefore important to include the impact of foreground as well as that of the inherent non-Gaussianity of the signal to make realistic predictions, and we defer these tasks for our future work.

Table 3. Maximum SNR achievable ($SNR_{\rm max}$) per frequency channel for the three instruments at $\ell \sim 550$ with 1000 h of observations. We also show $SNR_{\rm int}$ integrated within 5 MHz frequency-width around frequencies at which $\mathcal{D}_\ell(\nu, \nu)$ peaks, i.e. $\nu_{\rm p}$.

Telescope	$SNR_{\rm max}$ (per channel)	Peak freq. ($\nu_{\rm p}$ in MHz)	$SNR_{\rm int}$ (5 MHz)
HERA	5.9	105	6.2
NenuFAR	3.0	67.5	5.5
SKA-Low	6.4	105	6.5

ACKNOWLEDGEMENTS

AKS, RG, and SZ acknowledge support by the Israel Science Foundation (grant no. 255/18). RM is supported by the Israel Academy of Sciences and Humanities & Council for Higher Education Excellence Fellowship Program for International Postdoctoral Researchers. GM acknowledges support by Swedish Research Council grant 2020–04691. FM acknowledges support of the PSL Fellowship. LVEK acknowledges the financial support from the European Research Council (ERC) under the European Union's Horizon 2020 research and innovation programme (Grant agreement No. 884760,'CoDEX'). The authors thank the anonymous referee for the constructive feedback.

DATA AVAILABILITY

The data underlying this article will be shared on reasonable request to the corresponding author.

REFERENCES

Abdurashidova Z. et al., 2022, ApJ, 925, 221
Ali S. S., Bharadwaj S., Chengalur J. N., 2008, MNRAS, 385, 2166
Bañados E. et al., 2018, Nature, 553, 473
Barkana R., Loeb A., 2006, MNRAS, 372, L43
Beardsley A. P. et al., 2016, ApJ, 833, 102
Becker R. H. et al., 2001, AJ, 122, 2850
Becker G. D., Bolton J. S., Madau P., Pettini M., Ryan-Weber E. V., Venemans B. P., 2015, MNRAS, 447, 3402

Behroozi P. S., Silk J., 2015, ApJ, 799, 32
Berk D. E. V. et al., 2001, AJ, 122, 549
Bernardi G. et al., 2010, A&A, 522, A67
Bernardi G. et al., 2009, A&A, 500, 965
Bharadwaj S., Pandey S. K., 2005, MNRAS, 358, 968
Bharadwaj S., Sethi S. K., 2001, JA&A, 22, 293
Bharadwaj S., Pal S., Choudhuri S., Dutta P., 2018, MNRAS, 483, 5694
Cheng C. et al., 2018, ApJ, 868, 26
Choudhuri S., Bharadwaj S., Ghosh A., Ali S. S., 2014, MNRAS, 445, 4351
Dai W.-M., Ma Y.-Z., Guo Z.-K., Cai R.-G., 2019, Phys. Rev. D, 99, 043524
Datta A., Bowman J. D., Carilli C. L., 2010, ApJ, 724, 526
Datta K. K., Mellema G., Mao Y., Iliev I. T., Shapiro P. R., Ahn K., 2012, MNRAS, 424, 1877
Datta K. K., Jensen H., Majumdar S., Mellema G., Iliev I. T., Mao Y., Shapiro P. R., Ahn K., 2014, MNRAS, 442, 1491
Davies F. B. et al., 2018, ApJ, 864, 142
DeBoer D. R. et al., 2017, PASP, 129, 045001
Dewdney P. E., Braun R., 2016, SKA1-Low Configuration Coordinates – Complete Set, https://www.skao.int/sites/default/files/documents/d18-SKA-TEL-SKO-0000422_02_SKA1_LowConfigurationCoordinates-1.pdf
Dixon K. L., Iliev I. T., Mellema G., Ahn K., Shapiro P. R., 2015, MNRAS, 456, 3011
Ďurovčíková D., Katz H., Bosman S. E. I., Davies F. B., Devriendt J., Slyz A., 2020, MNRAS, 493, 4256
Eastwood M. W. et al., 2019, AJ, 158, 84
Fagnoni N., de Lera Acedo E., Drought N., DeBoer D. R., Riley D., Razavi-Ghods N., Carey S., Parsons A. R., 2021, IEEE Trans. Antennas Propag., 69, 8143
Faisst A. L., Capak P., Carollo C. M., Scarlata C., Scoville N., 2014, ApJ, 788, 87
Fan X. et al., 2006, AJ, 132, 117
Feldman H. A., Kaiser N., Peacock J. A., 1994, ApJ, 426, 23
Field G. B., 1958, Proc. IREE Aust., 46, 240
Fioc M., Rocca-Volmerange B., 1997, A&A, 326, 950
Fixsen D. J. et al., 2011, ApJ, 734, 5
Furlanetto S. R., Peng Oh S., Briggs F. H., 2006, Phy. Rep., 433, 181
Gaikwad P. et al., 2020, MNRAS, 494, 5091
Gallerani S., Choudhury T. R., Ferrara A., 2006, MNRAS, 370, 1401
Gan H. et al., 2023, A&A, 669, A20
Gehlot B. K. et al., 2019, MNRAS, 488, 4271
Ghara R., Choudhury T. R., Datta K. K., 2015a, MNRAS, 447, 1806
Ghara R., Datta K. K., Choudhury T. R., 2015b, MNRAS, 453, 3143
Ghara R., Choudhury T. R., Datta K. K., Choudhuri S., 2016, MNRAS, 464, 2234
Ghara R., Mellema G., Giri S. K., Choudhury T. R., Datta K. K., Majumdar S., 2018, MNRAS, 476, 1741
Ghara R. et al., 2020, MNRAS, 493, 4728
Ghara R., Giri S. K., Ciardi B., Mellema G., Zaroubi S., 2021, MNRAS, 503, 4551
Ghosh A., Prasad J., Bharadwaj S., Ali S. S., Chengalur J. N., 2012, MNRAS, 426, 3295
Giri S. K., D'Aloisio A., Mellema G., Komatsu E., Ghara R., Majumdar S., 2019, J. Cosmol. Astropart. Phys., 2019, 058
Greig B., Trott C. M., Barry N., Mutch S. J., Pindor B., Webster R. L., Wyithe J. S. B., 2020a, MNRAS, 500, 5322
Greig B. et al., 2020b, MNRAS, 501, 1
Greig B., Mesinger A., Davies F. B., Wang F., Yang J., Hennawi J. F., 2022, MNRAS, 512, 5390
Gupta Y. et al., 2017, Curr. Sci., 113, 707
Harker G. J. A. et al., 2009, MNRAS, 393, 1449
Harnois-Déraps J., Pen U.-L., Iliev I. T., Merz H., Emberson J. D., Desjacques V., 2013, MNRAS, 436, 540
Hinshaw G. et al., 2013, ApJS, 208, 19
Hoag A. et al., 2019, ApJ, 878, 12
Hogan C. J., Rees M. J., 1979, MNRAS, 188, 791
Hothi I. et al., 2020, MNRAS, 500, 2264
Hu E. M., Cowie L. L., Barger A. J., Capak P., Kakazu Y., Trouille L., 2010, ApJ, 725, 394
Ishigaki M., Kawamata R., Ouchi M., Oguri M., Shimasaku K., Ono Y., 2018, ApJ, 854, 73
Islam N., Ghara R., Paul B., Choudhury T. R., Nath B. B., 2019, MNRAS, 487, 2785
Kern N. S., Parsons A. R., Dillon J. S., Lanman A. E., Fagnoni N., de Lera Acedo E., 2019, ApJ, 884, 105
Kolopanis M. et al., 2019, ApJ, 883, 133
Koopmans L. et al., 2014, Advancing Astrophysics with the Square Kilometre Array, SKA Organisation, p. 001
Kulkarni G., Keating L. C., Haehnelt M. G., Bosman S. E. I., Puchwein E., Chardin J., Aubert D., 2019, MNRAS, 485, L24
Li W. et al., 2019, ApJ, 887, 141
McGreer I. D., Mesinger A., D'Odorico V., 2014, MNRAS, 447, 499
McKinley B. et al., 2018, MNRAS, 481, 5034
Madau P., Meiksin A., Rees M. J., 1997, ApJ, 475, 429
Mao Y., Shapiro P. R., Mellema G., Iliev I. T., Koda J., Ahn K., 2012, MNRAS, 422, 926
Mason C. A., Treu T., Dijkstra M., Mesinger A., Trenti M., Pentericci L., de Barros S., Vanzella E., 2018, ApJ, 856, 2
Mellema G. et al., 2013, Exp. Astron., 36, 235
Mertens F. G., Ghosh A., Koopmans L. V. E., 2018, MNRAS, 478, 3640
Mertens F. G. et al., 2020, MNRAS, 493, 1662
Mertens F. G., Semelin B., Koopmans L. V. E., 2021, in Siebert A., Baillié K., Lagadec E., Lagarde N., Malzac J., Marquette J.-B., N'Diaye M., Richard J., Venot O., eds, SF2A-2021: Proceedings of the Annual Meeting. French Society of Astronomy and Astrophysics, Paris, p. 211
Mesinger A., Ferrara A., Spiegel D. S., 2013, MNRAS, 431, 621
Mevius M. et al., 2021, MNRAS, 509, 3693
Mineo S., Gilfanov M., Sunyaev R., 2012, MNRAS, 419, 2095
Mitra S., Choudhury T. R., Ratra B., 2018, MNRAS, 479, 4566
Mondal R., Bharadwaj S., Majumdar S., Bera A., Acharyya A., 2015, MNRAS, 449, L41
Mondal R., Bharadwaj S., Majumdar S., 2016, MNRAS, 456, 1936
Mondal R., Bharadwaj S., Majumdar S., 2017, MNRAS, 464, 2992
Mondal R., Bharadwaj S., Datta K. K., 2018, MNRAS, 474, 1390
Mondal R., Bharadwaj S., Iliev I. T., Datta K. K., Majumdar S., Shaw A. K., Sarkar A. K., 2019, MNRAS, 483, L109
Mondal R., Shaw A. K., Iliev I. T., Bharadwaj S., Datta K. K., Majumdar S., Sarkar A. K., Dixon K. L., 2020a, MNRAS, 494, 4043
Mondal R. et al., 2020b, MNRAS, 498, 4178
Mondal R., Mellema G., Murray S. G., Greig B., 2022, MNRAS, 514, L31
Morales A. M., Mason C. A., Bruton S., Gronke M., Haardt F., Scarlata C., 2021, ApJ, 919, 120
Mozdzen T. J., Mahesh N., Monsalve R. A., Rogers A. E. E., Bowman J. D., 2018, MNRAS, 483, 4411
Naidu R. P., Tacchella S., Mason C. A., Bose S., Oesch P. A., Conroy C., 2020, ApJ, 892, 109
Ota K. et al., 2017, ApJ, 844, 85
Paciga G. et al., 2011, MNRAS, 413, 1174
Paciga G. et al., 2013, MNRAS, 433, 639
Parsons A. R. et al., 2010, AJ, 139, 1468
Patil A. H. et al., 2017, ApJ, 838, 65
Planck Collaboration VI, 2020, A&A, 641, A6
Plante P. L., Battaglia N., Natarajan A., Peterson J. B., Trac H., Cen R., Loeb A., 2014, ApJ, 789, 31
Platania P., Bensadoun M., Bersanelli M., Amici G. D., Kogut A., Levin S., Maino D., Smoot G. F., 1998, ApJ, 505, 473
Pober J. C. et al., 2013, ApJ, 768, L36
Pritchard J. R., Furlanetto S. R., 2007, MNRAS, 376, 1680
Qin Y., Mesinger A., Bosman S. E. I., Viel M., 2021, MNRAS, 506, 2390
Raste J., Kulkarni G., Keating L. C., Haehnelt M. G., Chardin J., Aubert D., 2021, MNRAS, 507, 4684
Reich P., Reich W., 1988, A&AS, 74, 7
Reiman D. M., Tamanas J., Prochaska J. X., Ďurovčíková D., 2020, preprint (arXiv:2006.00615)

Robertson B. E., Ellis R. S., Furlanetto S. R., Dunlop J. S., 2015, ApJ, 802, L19
Rogers A. E. E., Bowman J. D., 2008, AJ, 136, 641
Santos S., Sobral D., Matthee J., 2016, MNRAS, 463, 1678
Scott D., Rees M. J., 1990, MNRAS, 247, 510
Shaw A. K., Bharadwaj S., Mondal R., 2019, MNRAS, 487, 4951
Shaw A. K. et al., 2023, JA&A, 44, 4
Shimabukuro H., Yoshiura S., Takahashi K., Yokoyama S., Ichiki K., 2015, MNRAS, 451, 467
Sobacchi E., Mesinger A., 2015, MNRAS, 453, 1843
Spinelli M., Bernardi G., Garsden H., Greenhill L. J., Fialkov A., Dowell J., Price D. C., 2021, MNRAS, 505, 1575
Sun G., Furlanetto S. R., 2016, MNRAS, 460, 417
Sunyaev R. A., Zeldovich Y. B., 1972, A&A, 20, 189
Swarup G., Ananthakrishnan S., Kapahi V. K., Rao A. P., Subrahmanya C. R., Kulkarni V. K., 1991, Curr. Sci., 60, 95
The HERA Collaboration et al., 2022, preprint (arXiv:2210.04912)
Thyagarajan N. et al., 2020, Phys. Rev. D, 102, 022002
Tingay S. J. et al., 2013, Publ. Astron. Soc. Aust., 30, e007
Trott C. M. et al., 2020, MNRAS, 493, 4711
Trott C. M., Mondal R., Mellema G., Murray S. G., Greig B., Line J. L. B., Barry N., Morales M. F., 2022, A&A, 666, A106
van Haarlem M. P. et al., 2013, A&A, 556, A2
Vignali C., Brandt W. N., Schneider D. P., 2003, AJ, 125, 433
Wang F. et al., 2020, ApJ, 896, 23
Watson W. A., Iliev I. T., D'Aloisio A., Knebe A., Shapiro P. R., Yepes G., 2013, MNRAS, 433, 1230
White M., Carlstrom J. E., Dragovan M., Holzapfel W. L., 1999, ApJ, 514, 12
Wold I. G. B. et al., 2022, ApJ, 927, 36
Wouthuysen S. A., 1952, AJ, 57, 31
Yang J. et al., 2020, ApJ, 897, L14
Zaldarriaga M., Furlanetto S. R., Hernquist L., 2004, ApJ, 608, 622
Zarka P., Coffre A., Denis L., Dumez-Viou C., Girard J., Grießmeier J.-M., Loh A., Tagger M., 2018, in Proceedings of the 2018 2nd URSI Atlantic Radio Science Meeting (AT-RASC). IEEE, Gran Canaria, Spain, p. 1
Zaroubi S., 2013, The Epoch of Reionization. Springer, Berlin, p. 45
Zawada K., Semelin B., Vonlanthen P., Baek S., Revaz Y., 2014, MNRAS, 439, 1615
Zhu Y. et al., 2021, ApJ, 923, 223
Zhu Y. et al., 2022, ApJ, 932, 76

This paper has been typeset from a TEX/LATEX file prepared by the author.